View metadata, citation and similar papers at core.ac.uk

brought to you by CORE

provided by Edinburgh Research Explorer

THE UNIVERSITY of EDINBURGH

Edinburgh Research Explorer

Supercritical CO2 behaviour during water displacement in a sandstone core sample

Citation for published version:
Al-zaidi, E, Fan, X & Edlmann, K 2018, 'Supercritical CO2 behaviour during water displacement in a sandstone core sample', *International Journal of Greenhouse Gas Control*, vol. 79, pp. 200-211. https://doi.org/10.1016/j.ijggc.2018.11.005

Digital Object Identifier (DOI):
10.1016/j.ijggc.2018.11.005

Link:
Link to publication record in Edinburgh Research Explorer

Document Version:
Peer reviewed version

Published In:
International Journal of Greenhouse Gas Control

General rights
Copyright for the publications made accessible via the Edinburgh Research Explorer is retained by the author(s) and / or other copyright owners and it is a condition of accessing these publications that users recognise and abide by the legal requirements associated with these rights.

Take down policy
The University of Edinburgh has made every reasonable effort to ensure that Edinburgh Research Explorer content complies with UK legislation. If you believe that the public display of this file breaches copyright please contact openaccess@ed.ac.uk providing details, and we will remove access to the work immediately and investigate your claim.

Download date: 02. Jan. 2020

Supercritical CO_2 Behaviour during Water Displacement in a Sandstone Core Sample

Ebraheam Al-Zaidi[a], Xianfeng Fan[a]*, Katriona Edlmann[b]

[a] Institute for Materials and Processes, School of Engineering, The University of Edinburgh, King's Buildings, Mayfield Road, Edinburgh, EH9 3JL, United Kingdom
[b] School of Geoscience, Grant Institute, The King's Buildings, The University of Edinburgh, James Hutton Road, Edinburgh EH9 3FE, United Kingdom.

* Corresponding author. Tel.: +44 0 131 6505678; fax: +44 0131 6506551. E-mail address: x.fan@ed.ac.uk (X.Fan).

Abstract: CO_2 injection into underground formations involves the flow of CO_2 in subsurface rocks which already contain water. The flow of CO_2 into the target formation is governed mainly by capillary forces, viscous forces and interfacial interactions. Any change in subsurface conditions of pressure and temperature during injection will have an impact on the capillary and viscous forces and the interfacial interactions, which, in turn, will have an influence the injection, displacement, migration, and storage capacity and security of CO_2. In this study, an experimental investigation has been designed to explore the impact of fluid pressure (74-90 bar), temperature (33-55 °C), and injection rate (0.1-1 ml/min) on the dynamic pressure evolution and displacement efficiency when supercritical CO_2 is injected into a water-saturated sandstone core sample. The study also highlights the impact of the capillary forces and viscous forces on the two-phase flow characteristics and shows the conditions where capillary forces or viscous forces become dominant. The authors are not aware of similar experimental studies conducted in the literature so far. The results revealed a moderate to considerable impact of the parameters investigated on the differential pressure profile, cumulative produced volumes, endpoint CO_2 relative (effective) permeability and residual water saturation. The extent of the impact of each parameter (e.g. fluid pressure) was a function of the associated parameters (e.g. temperature and injection rate). Increasing fluid pressure caused the differential pressure profile of supercritical CO_2-water displacement to transform to the likeness of liquid CO_2-water displacement, while, increasing temperature transforms it to the likeness of gaseous CO_2-water displacement. Increasing fluid pressure caused a considerable reduction in the maximum and quasi-differential pressures, an increase in the endpoint CO_2 relative permeability (K_{rCO2}) and a reduction in the residual water saturation (S_{wr}) and

cumulative produced volumes. Overall, the impact of temperature is opposite to that of fluid pressure. However, with increasing temperature, the K_{rCO2} showed a declining trend at high-fluid pressures (90 bar) but an increasing trend at low-fluid pressures (75 bar). Increasing injection rate caused a considerable increase in the maximum and quasi-differential pressures, a rise in the K_{rCO2}, a reduction in the S_{wr}, and an increase in the cumulative produced volumes. The S_{wr} was in range of 0.34-0.41 while K_{rCO2} was less than 0.37, depending on the operational conditions. Changing the operational conditions caused a higher impact on K_{rCO2} than that on S_{wr}. The results indicate that capillary forces dominate the multiphase flow characteristics as fluid pressure and temperature are increased.

1 Introduction

The storage of carbon dioxide in deep saline aquifers, abounded or depleted oil and gas reservoirs (Delshad et al., 2010; Gozalpour et al., 2005; Kaveh et al., 2012), and unminable coal bed seams (Kaveh et al., 2012; Plug and Bruining, 2007a) is increasingly viewed as a promising technology to mitigate the increasing emissions of anthropogenic CO_2 into the atmosphere due to fossil fuel burning and other human activities (Bachu, 2001; Hangx et al., 2013; Kazemifar et al., 2015), enhance hydrocarbon recovery or extract geothermal heat (Kaveh et al., 2012; Tutolo et al., 2015).

During the injection process, supercritical (Sc) CO_2 will displace formation water in an immiscible drainage displacement process (Bachu, 2000; Basbug et al., 2005). The multiphase flow properties are controlled by the interplay of many factors including capillary forces, viscous forces, gravity forces (Roof, 1970; Rostami et al., 2010), interfacial interactions, solubility of CO_2 in formation water, phase densities and viscosities of the injected and present fluids, petrophysical properties of the aquifer, and injection rate and its duration (Pentland et al., 2011). Due to the small pore sizes of subsurface rocks and sands, the capillary forces at the CO_2-water interface will have a considerable influence on the two-phase flow through a porous medium (Roof, 1970). The interplay between the capillary forces, viscous forces as well as gravity forces governs the displacement front behaviour, which potentially has an impact on fluids distribution, in turn, will have a potential influence on the macroscopic transport

characteristics such as relative permeability and capillary pressure (Rostami et al., 2010). Change in fluid pressure, temperature, and injection rate will have a direct impact on most of the aforementioned factors; therefore, changing the operational conditions will have a moderate to significant influence on the injectivity (Müller, 2011), migration, storage and long-term integrity efficiency of CO_2 processes (Saraji et al., 2013). The CO_2 injectivity is a key factor in determining the amount, pace, and period of CO_2 injection in a saline aquifer (Mijic et al., 2014).

Multiphase flow corresponding with CO_2 injection into subsurface formations is a complex process, thus conducting core-scale displacements under a wide range of parameters (e.g. different pressure, temperature and injection rate conditions) will provide us with a deeper understanding of the behaviour of immiscible flow through natural porous media, thereby enabling us to build models that approximate physics more closely (Aryana and Kovscek, 2012). Despite its importance, the multiphase flow properties of CO_2-water (brine) systems are poorly investigated in comparison to CO_2-oil systems (Bahralolom et al., 1988; Perrin and Benson, 2010). Our literature review shows a large research effort has been allocated to CO_2 wettability (Al-Menhali and Krevor, 2014; Bikkina, 2011; Farokhpoor et al., 2013a; Kaveh et al., 2012; Li, 2015; Sakurovs and Lavrencic, 2011; Saraji et al., 2013; Yang et al., 2007) and CO_2 interfacial tension (Aggelopoulos et al., 2010; Bachu and Bennion, 2008, 2009; Busch and Müller, 2011; Chiquet et al., 2007; Li et al., 2012; Yu et al., 2012). Cinar and Riaz in their literature review pointed out the need to more investigations on multiphase flow characteristics of CO_2-(water) brine-solid systems (Cinar and Riaz, 2014).

The limited investigations of the multiphase flow characteristics of $ScCO_2$-(water) brine systems are mainly classified into computational modelling (Jobard et al., 2013; Ma et al., 2013; Mijic et al., 2014; Xu et al., 2011) and laboratory experiments (Berg et al., 2013; Levine et al., 2011; Pini et al., 2012; Song et al., 2012; Suekane et al., 2005; Zheng et al., 2017). The laboratory $ScCO_2$-brine (water) experiments have been conducted on various porous media that include synthetic and natural core samples (Berg et al., 2013; Edlmann et al., 2013; Levine et al., 2011; Pini et al., 2012), micromodels (Zheng et al., 2017), and packed bed of glass beads (Song et al., 2012; Suekane et al., 2005). In these experiments, researchers

82 investigated the multiphase flow properties by measuring various parameters that include: relative
83 permeability curves (Berg et al., 2013; Chang et al., 2013; Krevor et al., 2013; Suekane et al., 2005;
84 Suenaga and Nakagawa, 2011), capillary pressure curves (Herring et al., 2014; Wang et al., 2013), CO_2
85 residual saturation and distribution (Alemu et al., 2011; Chang et al., 2013; Herring et al., 2014; Pentland
86 et al., 2011; Saeedi et al., 2011; Suekane et al., 2005), heterogeneity impact (Ott et al., 2015; Perrin and
87 Benson, 2010; Shi et al., 2011; Wang et al., 2013), flow regimes (Armstrong et al., 2017), water
88 displacement efficiency (Cao et al., 2016), and formation dry out (Ott et al., 2011).

89 Nevertheless, despite the wide research on CO_2–water (brine) systems and despite its high
90 importance, the literature provided shows that the analysis of the pressure data in core flooding has
91 been widely overlooked (Rezaei and Firoozabadi, 2014). In this paper, laboratory dynamic drainage
92 experiments were performed by injecting pure CO_2 in its supercritical state into the core sample to
93 investigate the impact of fluid pressure, temperature and injection rate on the multiphase flow
94 characteristics, especially focusing on the differential pressure profile, water production profile,
95 residual water saturation, and endpoint effective and relative permeabilities of CO_2. One of the main
96 objectives of this investigation is to shed more light on the impact of capillary forces and viscous forces
97 on the two-phase flow characteristics and highlights the conditions at which the capillary forces or
98 viscous forces become dominant. To the authors' best knowledge, no such experimental investigation
99 has been conducted to explore the dynamic pressure evolution and displacement efficiency when
100 supercritical CO_2 is flooded into a deionised water-saturated sandstone core sample. The results of this
101 study would be of importance for evaluating CO_2 injectivity, fluid migration and entrapment,
102 displacement efficiency, CO_2 storage capacity (Levine et al., 2011; Wang et al., 2015), and efficiency and
103 integrity of the CO_2 sequestration processes (Busch and Müller, 2011; Rathnaweera et al., 2015).
104

2 Materials

The unsteady state dynamic drainage experiments ($ScCO_2$-water displacements) were conducted on a sandstone core sample from Guillemot A Field in the North Sea. The core sample used in this work is of 2.54 cm diameter and 7.62 cm length. The average porosity and absolute water permeability of the core sample are about 14% and 15.8 millidarcys, respectively. To calculate the core sample pore volume and porosity, the core was saturated with deionized water and then the weight difference between the dry and the wet core sample was used. This study is one in a series, therefore, the core sample description, core sample setup and CO_2-water displacements procedures can be found in Al-Zaidi et al. (Al-Zaidi et al., 2018b).

3 Results and Discussions

To gain a proper understanding of the two-phase flow characteristics of $ScCO_2$-water drainage displacements, the differential pressure profile, production profile, residual water saturation and endpoint relative and effective permeabilities of CO_2 were measured and analysed.

The differential pressure refers to the difference between the readings of the pressure transducers at the inlet and the outlet sides of the core sample. The capillary and viscous forces are the most influential forces that govern the differential pressure profile when CO_2 is injected in a horizontal direction. Espinoza and Santamarina related the capillary and viscous forces with the differential pressure (Espinoza and Santamarina, 2010) as follows:

$$\Delta P = P_{CO2} - P_{water} = 4\,\frac{\sigma_{CO_2-water}\,COS\theta}{d} + v\,\frac{32\,L}{d^2}\left(\frac{l_{CO_2}\mu_{CO_2}+l_{water}\mu_{water}}{L}\right) \quad (1)$$

where ΔP is the differential pressure across the core sample (Pa). P_{CO2} and P_{water} are the CO_2 phase and water bulk pressures, respectively; $\sigma_{CO2\text{-}water}$ is the CO_2-water interfacial tension (mN/m), θ the contact angle between fluids and core sample surface, d (m) the diameter of the largest effective pore (Chiquet et al., 2007; Farokhpoor et al., 2013b), v (m/sec) the fluid velocity in the pores, L (m) the length of the core sample, l (m) length of CO_2 or water phase inside the core sample, and μ (Pa·s) the viscosity

of the fluids. The first term of Eq.1 refers to the Young-Laplace equation, which accounts for the capillary forces, while the second term refers to the Poiseuille's equation (Espinoza and Santamarina, 2010; Li, 2015), which accounts for the viscous forces. The capillary forces which exist because of the presence of the CO_2-water interface inside pore network (Bikkina et al., 2016) govern the multiphase flow during immiscible displacements (Schembre and Kovscek, 2003) and leads to the trapping of one phase by another during immiscible displacements (Akbarabadi and Piri, 2013; Chatzis and Morrow, 1984). The capillary forces are determined by CO_2-water interfacial tension, wettability of the system as well as the core sample pore size distribution (Alkan et al., 2010; Bikkina et al., 2016; Chatzis and Morrow, 1984; Fulcher Jr et al., 1985). The viscous forces are governed by the injection rate, the viscosity of the displacing and displaced fluids, and the core sample properties such as cross sectional area, core sample length, and permeability.

In this study, the experimental data has been categorized into four main sections. The first three sections deal with the impact of fluid pressure (75-90 bar), temperature (33-55 °C) and injection rate (0.1- 1ml/min) on the differential pressure profile and production behaviour; while the fourth section deal with their influence on the endpoint CO_2 effective (relative) permeability and residual water saturation. It should be noted that during this study, the corresponding time refers to the time required to reach the maximum-differential pressure at the start of the experiment. The quasi-differential pressure refers to the differential pressure measured at the end of the core flooding. For the pump injection rates of 0.1, 0.4, 0.6, and 1 ml/min, the Darcy flux is around 0.0197, 0.079, 0.118, and 0.197 cm/min while the average linear velocity is around 0.141, 0.564, 0.846, and 1.41 cm/min. It is worth stating that for comparative purposes, we will maintain the use of injection rate from the pump as our reference "flowrate" in this study.

3.1 Effect of Fluid Pressure on the Differential Pressure Profile of $ScCO_2$-Water Displacements.

To have a thorough understanding about the effect of fluid pressure on the differential pressure and water recovery of $ScCO_2$-water displacements, experiments were conducted under various fluid

pressures (75-90 bar), temperatures (33 and 45 °C) and injection rates (0.1,0.4, and 1 ml/min). The discussion of the pressure data will be presented in two sections. The first section deals with experiments conducted at 33 °C while the second one deals with experiments performed at 45 °C.

3.1.1 Effect of Fluid Pressure on the Differential Pressure Profile of $ScCO_2$-Water Displacements Conducted at 33 °C.

The results from Figure 1-3 show that for all fluid pressures, the differential pressure increased sharply; then, it dropped steeply (under low pressure and high temperature conditions) or gradually (under high pressure and low temperature conditions) until it reached a nearly quasi-steady drop. Increasing fluid pressure caused a substantial drop in the maximum and quasi-differential pressures; the extent of this drop decreased as CO_2 injection rate increased. The reduction in the maximum differential pressure was always greater than the reduction in the quasi-differential pressure. The increase or a decrease in the corresponding time with increasing fluid pressure is dependent on the injection rate. Increasing fluid pressure led the differential pressure profile of the $ScCO_2$-water displacements to transform from the likeness of a gaseous CO_2 behaviour to a liquid-like CO_2 behaviour. It caused also a slight increase in the differential pressure profile of the 90 bar-experiment until it became slightly higher than the differential pressure profile of the 80 bar-experiment at the end of the displacements.

The data from Figure 1-3 present the effect of increasing fluid pressure on the differential pressure profile. The data shows that the profile of the differential pressure is characterized by a sharp increase that is followed by a strong or gradual reduction (depending on the pressure and temperature range) until it reached an almost quasi-steady profile. In general, a similar behaviour has been reported by Bikini et al. and Ott et al. (Bikkina et al., 2016; Ott et al., 2015). The sharp increase in the differential pressure occurred because the injected CO_2 entered the pore network of the sandstone core sample for the first time and had to overcome the entry pressure of the sandstone pore network. According to Eq.1, the strong reduction in the differential pressure can be attributed to the reduction in both capillary and viscous forces. The reduction in the capillary forces is expected to occur when capillary pore throats are

opened to flow, i.e. after CO_2 breakthrough (Kwelle, 2017). On the other hand, the reduction in the viscous forces can be associated with the replacement of a more viscous fluid (water) by a less viscous fluid (CO_2) and with the increase in the CO_2 relative permeability at the expense of water relative permeability (Chang et al., 2013).

The gas expansion effect can occur as a result of the change in the injected CO_2 density due to the temperature difference inside and outside the water bath (Carpenter, 2014; Perrin and Benson, 2010). During this study, the density of the injected CO_2 varies as the CO_2 enters the water bath. The density change, i.e. density ratio, is a function of the injection rate, fluid pressure and the temperature difference from the pump (under room temperature) to the core sample inside the water bath. The density ratio (d_r) suggested by Perrin and Benson (Perrin and Benson, 2010) has been used to calculate the volumetric injection rate inside the core sample. For instance, at a fluid pressure of 40 bar, an injection rate of 1 ml/min at 20 °C becomes 1.108 ml/min at 33 °C.

$$d_r = \frac{{d_{CO2}}^{20\,^{\circ}C,\ 40\ bars}}{{d_{CO2}}^{33^{\circ}C,\ 40\ bars}} \tag{3}$$

The data from Figure 1-3 reveal that the increase in the fluid pressure led to a considerable reduction in the maximum and quasi-differential pressures along with the increase or a decrease in the corresponding time depending on the injection rate; the corresponding time increased with increasing fluid pressure at an injection rate of 0.1 ml/min and decreased at an injection rate of 0.4 ml/min and higher. For illustration, the data from Figure 1 exhibits that as the fluid pressure increased (from 75 to 90 bar) at 0.1 ml/min injection rate, the maximum-differential pressure dropped by around 72% (from 0.36 to 0.102 bar) and the quasi-differential pressure decreased by around 69.5% (from 0.154 to 0.047 bar) but the corresponding time increased by around 66% (from 6.5 to 10.8 min). The data from Figure 2 shows that as the fluid pressure increased (from 75 to 90 bar) at 0.4 ml/min, the maximum-differential pressure dropped by around 46.6% (from 1.121 to 0.599 bar), the quasi-differential pressure declined by around 39% (from 0.363 to 0.221 bar), and the corresponding time reduced by around 68.4% (from 1.9 to 0.6 min). The data from Figure 3 shows that increasing the fluid pressure (from 75 to 80 and then

206 to 90 bar) at 1 ml/min, caused the maximum-differential pressure to drop by around 40% (from 2.492
207 to 1.496 bar), the quasi-differential pressure to decline by around 38% (from 0.994 to 0.614), and the
208 corresponding time to decline by around 15.6% (from 3.2 to 2.7 min).

209 The reduction in the differential pressure of supercritical CO_2-water systems is also observed by
210 us with supercritical CO_2-oil systems, for more information see Al-Zaidi et al. (Al-Zaidi et al., 2018a).
211 According to Eq.1, the reduction observed in the differential pressure profile is the net result of the
212 reduction in the capillary forces and the increase in the viscous forces with increasing fluid pressure.
213 The reduction in the capillary forces with increasing fluid pressure is due to the reduction in the CO_2-
214 water interfacial tension, as shown in Figure 4, and the increase in contact angle because of the increase
215 in CO_2 solubility (Jung and Wan, 2012; Plug and Bruining, 2007b; Yang et al., 2007). The increase in the
216 viscous forces with increasing fluid pressure is due to the increase in CO_2 viscosity (Peace software,
217 2017). For illustration, as the fluid pressure increased from 75 to 90 bar, the $ScCO_2$ viscosity increased
218 from 33.3095 to 53.837 × [10^{-6} (Pa·s)] (Peace software, 2017), and the CO_2-water interfacial tension (IFT)
219 reduced slightly, by around 3 Nm/m, from around 28 to 25 mN/m as shown in Figure 4 (Bachu and
220 Bennion, 2008). As a result, the reduction observed in the differential pressure with increasing fluid
221 pressure might be related mainly to the increase in contact angle. This is in agreement with the findings
222 by Yang et al. (Yang et al., 2005), Liu et al. (Liu et al., 2010), and Jung and Wan (Jung and Wan, 2012).
223 Yang et al. (Yang et al., 2005) and Liu et al. (Liu et al., 2010) noticed that using a supercritical CO_2 phase
224 with reservoir rocks leads to a higher alteration towards less water-wetting status compared to gaseous
225 and liquid CO_2 phases. Moreover, Jung and Wan (Jung and Wan, 2012) found that contact angle
226 increases significantly with increasing fluid pressure up to 100 bar when the fluid pressure is higher
227 than the critical pressure of CO_2 (larger than 73.8 bar) but remains fairly constant when the fluid
228 pressure is less than the critical pressure or above 100 bar.

229 Regarding the change in the corresponding time, the increase observed in the corresponding time
230 at low injection rate (0.1 ml/min) can be linked to the transformation of a supercritical CO_2-water
231 behaviour to a liquid-like CO_2-water behaviour; this transformation can result in reducing the mobility

232 ratio and the expansion impact effect due to the low sensitive nature of liquid CO_2 to pressure and
233 temperature change, more discussion will follow later. However, the reduction in the corresponding
234 time with higher injection rate (0.4 ml/min) is likely to be related to the reduction in the magnitude of
235 the maximum differential pressure with increasing fluid pressure.

236 The data from Figure 1-2 showed that the drop in the maximum-differential pressure with
237 increasing fluid pressure was always higher than that in the quasi-differential pressure. This can be
238 related to fact that the dynamic reduction in both capillary and viscous forces at the end of the
239 displacement is less than that at the start of the displacement.

240 The results from Figure 1-2 showed also that as the CO_2 injection rate increased, the reduction in
241 the differential pressure, due to increasing fluid pressure, decreased. This is because the reduction
242 observed in the differential pressure profile is the net result of the increase in the viscous forces and the
243 reduction in the capillary forces with increasing fluid pressure. Thus, with increasing injection rate, the
244 contribution of the viscous forces to the net pressure drop increase while the contribution of the
245 capillary forces decreases (Rezaei and Firoozabadi, 2014), thereby leading to a less reduction in the
246 differential pressure.

247

248 The data from Figure 1-2 show also that as the fluid pressure increased, the differential pressure
249 profile of the $ScCO_2$-water displacements transformed from the likeness of a gaseous CO_2 behaviour to
250 a liquid CO_2 behaviour; this transformation occurs at lower-fluid pressures with increasing injection
251 rate. For instance, the differential pressure profile of the 75 bar-experiment is very similar to that of a
252 typical high-fluid pressure gaseous CO_2-water displacement while that of 90 bar-experiment is virtually
253 identical to that of a typical liquid CO_2-water displacement (Al-Zaidi et al., 2018b). Increasing the CO_2
254 injection rate from 0.1 to 0.4 ml/min caused the transition from a gaseous to liquid CO_2 behaviour to
255 occur at lower fluid pressure. For the 0.1 ml/min-displacements, the transition towards liquid CO_2
256 behaviour occurred at 90 bar. Nonetheless, for the 0.4 ml/min-displacements, it started from 77 bar. The
257 similarity to a gaseous or a liquid CO_2 behaviour has been decided mainly on the rate of reduction in

the differential pressure profile during early times of flooding; the gaseous CO_2 displacements are characterized by a high-pressure drop at early stages while the liquid CO_2 displacements are characterized by a slight drop (Al-Zaidi et al., 2018b). The transformation of the differential pressure profile at low pressures with increasing injection rate can be related to the increase in viscous pressure drop (with increasing injection rate) that leads to a reduction in the total pressure drop (as stated above); this, in turn, caused the appearance of the liquid CO_2 like differential pressure profile, which is characterized by a gradual pressure drop at early stages.

The transformation of the differential pressure profile with increasing fluid pressure proposes that the capillary and viscous properties of a supercritical CO_2 phase become similar to that of gaseous CO_2 phase at low fluid pressures and similar to that of liquid CO_2 phase at high fluid pressures; liquid CO_2 is characterized by higher viscous forces and lesser capillary forces compared to gaseous CO_2. With increasing fluid pressure, the viscous forces of supercritical CO_2 phase become higher while the capillary forces become lesser. This is because the increase in the fluid pressure leads to the increase in the CO_2 viscosity as well as the decrease in the interfacial tension and the increase in the contact angle due to the increasing CO_2 solubility (Espinoza and Santamarina, 2010; Plug and Bruining, 2007a). Moreover, the transformation towards liquid CO_2 behaviour might have occurred because the wettability behaviour of liquid and supercritical CO_2 phases become very close to each other at high-pressure conditions. The wettability of the core sample with supercritical and liquid CO_2 might have been altered towards hydrophobic wetting status at high pressures. This potential wettability alteration might have occurred due to the fluid pressure increase in case of supercritical CO_2 (Jung and Wan, 2012; Yang et al., 2005) (as illustrated above), and CO_2 phase transformation in case of liquid CO_2 (Yang et al., 2007). Yang et al. observed that as gaseous CO_2 phase transforms to liquid CO_2, the wetting status becomes hydrophobic (Yang et al., 2007).

The data from Figure 1 show that after about 170 min, the differential pressure profile of the 90 bar-experiment experienced a gradual increase until it became slightly higher than the differential

pressure profile of the 80 bar-experiment. The reason is not entirely clear. However, the first possible explanation is that as water depletion progressed and, hence, the viscous pressure drop across the core sample diminished, the flow of CO_2 through non-depleted capillaries was partially blocked by the capillary forces (Nutt, 1982), more discussion can be seen in in Al-Zaidi et al. (Al-Zaidi et al., 2018a; Al-Zaidi et al., 2018b). As a result, the pressure of the CO_2 had to build up to a certain level to overcome the capillary forces (Hildenbrand et al., 2002; Nutt, 1982). The second possible explanation is that, after around 170 min, the impact of viscous forces became higher than that of capillary forces as most of the water was displaced; thereby CO_2 was flowing through opened pores. The result was less impact for capillary forces (Kwelle, 2017).

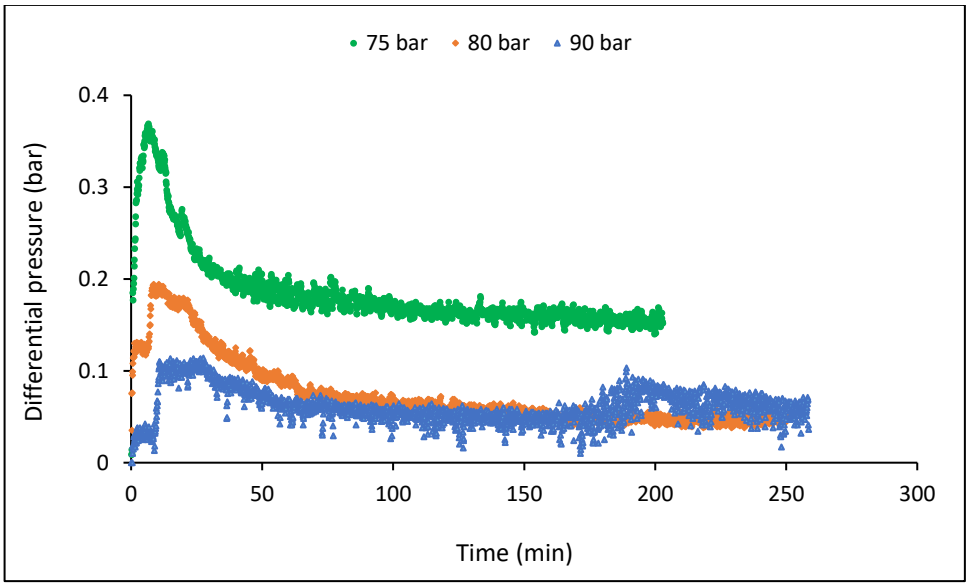

Figure 1: Effect of fluid pressure on the differential pressure profile of $ScCO_2$-water displacements conducted at 0.1 ml/min and 33 °C.

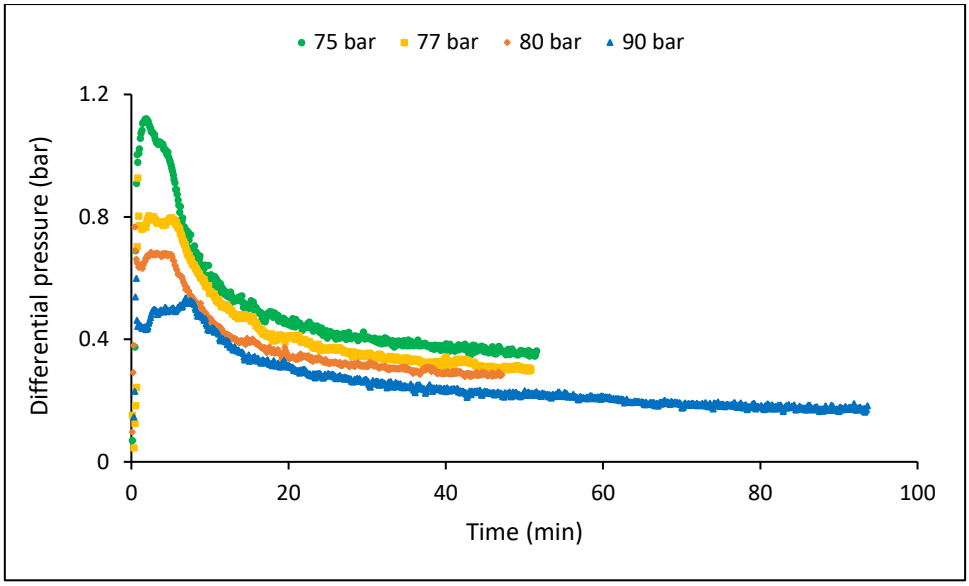

295

296 Figure 2: Effect of fluid pressure on the differential pressure profile of $ScCO_2$-water displacements
297 conducted at 0.4 ml/min and 33 °C.

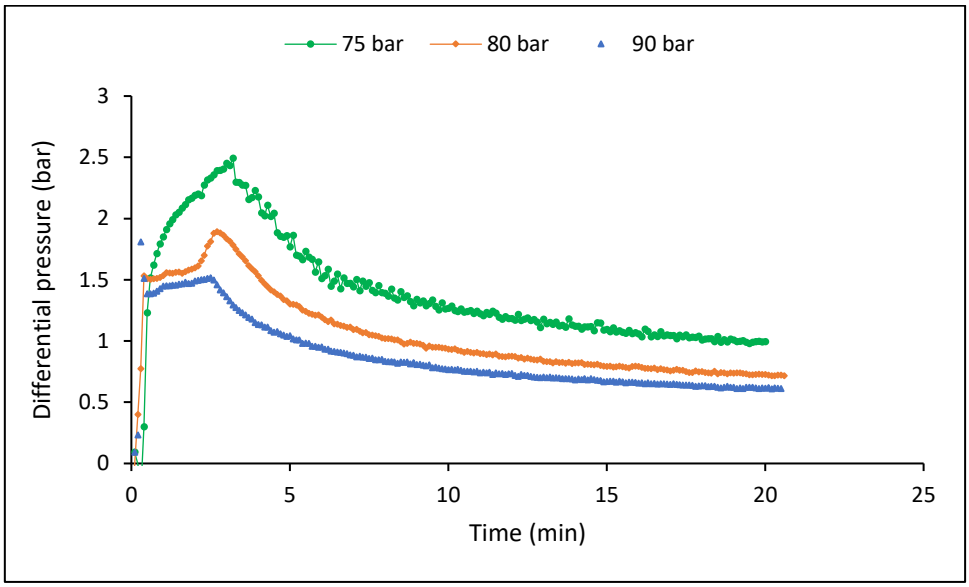

298

299 Figure 3: Effect of fluid pressure on the differential pressure profile of $ScCO_2$-water displacements
300 conducted at 1 ml/min and 33 °C.

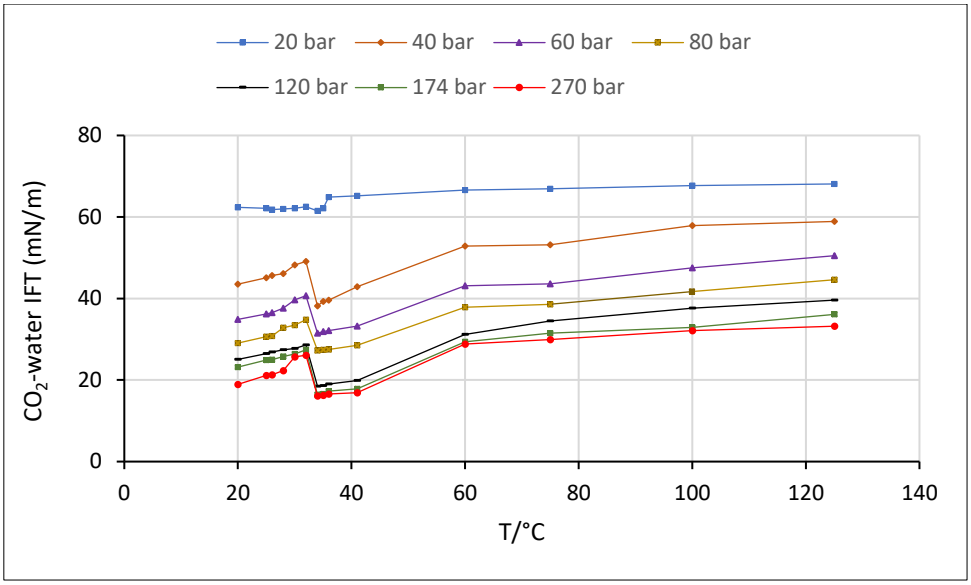

Figure 4: Experimental interfacial tension for CO_2-Pure Water Systems adopted from (Bachu and Bennion, 2008).

3.1.2 *Effect of Fluid Pressure on the Differential Pressure Profile of ScCO₂-Water Displacements Conducted at Higher Temperatures (45 °C).*

Figure 5 presents the effect of increasing fluid pressure on the differential pressure at a higher temperature (45 °C). Overall, in comparison to experiments conducted under lower temperature (33 °C) conditions, the differential pressure profile of the higher temperature (45 °C) displacements becomes more similar to gaseous CO_2 behaviour than liquid CO_2 behaviour.

The data from Figure 5 reveals also that the differential pressure profile experienced the highest reduction within the first three to five minutes of running the experiments and reached a quasi-pressure state after around 20 min. This indicates that most of the water recovery happened during the first five minutes of running the coreflooding. As a result, the differential pressure profile of the 80 and 90 bar became almost identical after 3.3 min. These nearly identical pressure profiles might have occurred because the reduction in the differential pressure profile (due to the decline of the capillary forces with increasing pressure) was equalled by the increase in the differential pressure profile (owing to the increase of the viscous forces with increasing pressure). This suggests that in comparison to capillary forces, the viscous forces played a vital role at later stages of the displacements. During these stages, it is expected that the bypassed water was concentrated inside the smallest pores and the larger pores

were occupied by the injected CO_2 (Chang et al., 2013). Consequently, the impact of the capillary forces was significantly reduced (Kwelle, 2017).

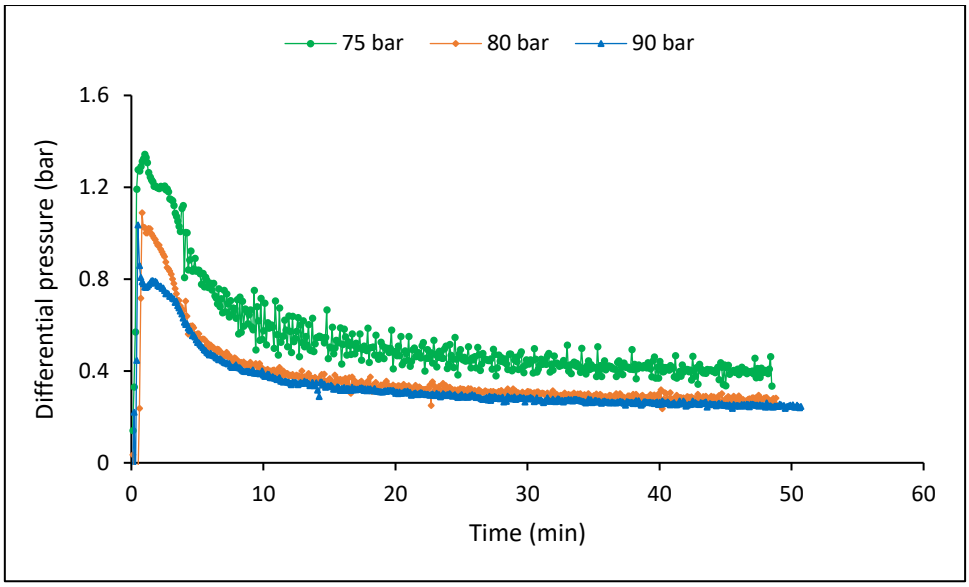

Figure 5: Effect of fluid pressure on the differential pressure profile of $ScCO_2$-water displacements conducted at 0.4 ml/min, and 45 °C.

3.1.3 *Effect of Temperature on the Differential Pressure Profile of $ScCO_2$-Water Drainage Displacements.*

To have a deep understanding of the effect of temperature on the differential pressure and water recovery of $ScCO_2$-water displacements, a series of experiments were conducted under different temperatures (33 and 45 °C), different injection rates (0.1, 0.4, and 1ml/min), and different fluid pressures (75-90 bar) conditions.

The data from Figure 6-9 show that increasing temperature caused the differential pressure profile to transform to the likeness of gaseous CO_2 behaviour. Increasing temperature caused a significant increase in the maximum and quasi-differential pressures; the extent of this increase increased with the injection rate. The corresponding time decreases or increases depending on the CO_2 injection rate. Increasing temperature at a lower fluid pressure (75 bar) led to the appearance of the differential pressure oscillations in addition to the increase in the maximum and quasi-differential pressures.

The data from Figure 6-9 show the effect of increasing temperature on the differential pressure at different fluid pressures and injection rates. Contrary to the fluid pressure effects, the increase in temperature, from 33 to 45 °C at 90 bar, caused the differential pressure profile to transform to the likeness of gaseous CO_2 behaviour, as shown in Figure 6. The increase in temperature produced a notable increase in the maximum and quasi-differential pressures; the extent of this increase increased with the injection rate. The reduction or increase in the corresponding time is dependent on the CO_2 injection rate; the corresponding time decreased with increasing temperature at an injection rate of 0.1 ml/min and increased with increasing temperature at an injection rate of 0.4 ml/min and higher; which is opposite to the impact of fluid pressure as stated above. For illustration, the data from Figure 6 shows that as the temperature increased (from 33 to 45 °C) at 0.1 ml/min and 90 bar, the maximum-differential pressure increased by around 133% (from around 0.11 to 0.256 bar) but the corresponding times dropped by around 44.5% (from around 11 to 6.1 min). The quasi-differential pressure was almost identical, apart from the gradual increase of the differential pressure profile after about 170 min, see Section 3.1.1 above for more information. The data from Figure 7 shows that increasing the temperature (from 33 to 55 °C) at 0.4 ml/min and 90 bar, caused the maximum-differential pressure to rise by around 75.5% (from 0.599 to 1.051 bar), the quasi-differential pressure to increase by 54% (from 0.224 to 0.345 bar), and the corresponding time to extend by around 17% (from 0.6 to 0.7 ml/min). The corresponding time of both 33 and 45 °C-displacements was equal and their differential profiles were almost identical during the last period. The data from Figure 8 shows that for the displacements conducted at 1 ml/min and 90 bar, increasing the temperature (from 33 to 55 °C) led the maximum-differential pressure to increase by around 246.6% (from 0.786 to 2.724 bar), the quasi-differential pressure to increase by about 201% (from 0.299 to 0.901 bar), and the corresponding time to extend by 47% (from 1.7 to 2.5 min).

According to Eq.1, the increase observed in the differential pressure profile with increasing temperature can be related mainly to the increase in the capillary forces and slightly to the increase in the applied viscous forces. The increase in the capillary forces with increasing temperature is due to the increase in the CO_2-water interfacial tension and the reduction in the contact angle because of the

reduction in CO_2 solubility (Bachu and Bennion, 2008; Yang et al., 2007). On the other hand, the slight increase in the viscous forces with increasing temperature, despite the reduction in the CO_2 dynamic viscosity, is because of increasing the CO_2 injection rate due to expansion impact. For the experiments conducted at 90 bar-0.4 ml/min, as the temperature increased from 33 to 55 °C, the IFT increased from 25 to 28 mN/m and the CO_2 injection rate inside the core sample increased from 0.506 to 1.296 ml/min but the CO_2 viscosity decreased from 53.837 to 22.26 × [10^{-6} (Pa·s)](Peace software, 2017).

The results from Figure 9 show the effect of increasing temperature on the differential pressure at a lower fluid pressure (75 bar). Increasing temperature from 33 to 45 °C led to the appearance of the differential pressure oscillations for the first time. As the temperature further increased to 55 °C, the magnitude of the oscillations increased. Moreover, increasing temperature from 33 to 55 °C caused the maximum-differential pressure to increase by around 29% (from 1.12 to 1.444 bar), the quasi-differential pressure to increase by about 21% (from 0.367 to 0.444 bar) and the corresponding times to prolong by 175% (from 1 to 1.17 min). The differential pressure oscillations are likely to appear because of the reduction in the ratio of the viscous forces to capillary forces. Thus, the capillary forces became higher than the viscous forces and; a result, the water flow paths were closed (Nutt, 1982).

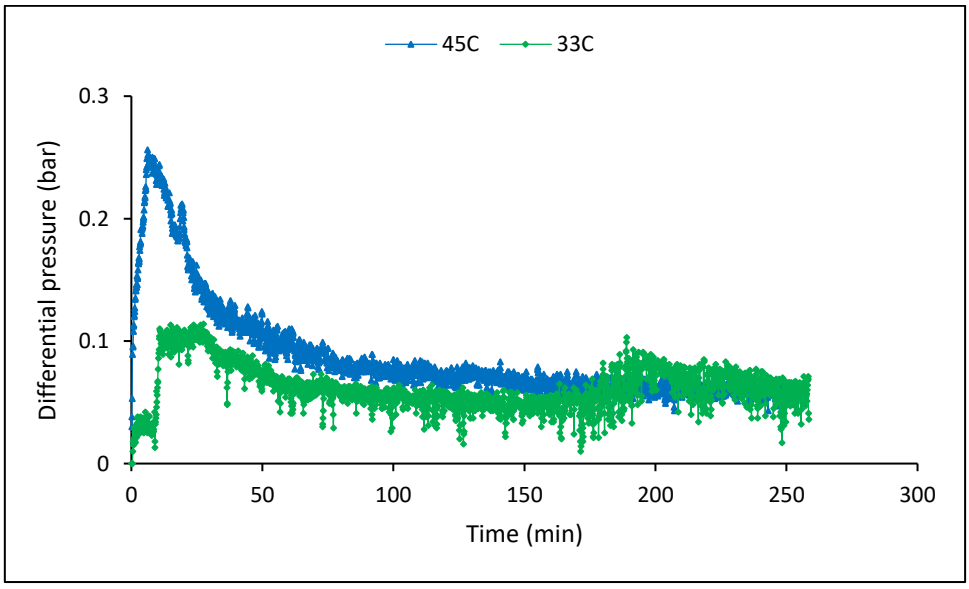

Figure 6: Effect of temperature on the differential pressure profile of $ScCO_2$-water displacements conducted at 90 bar and 0.1 ml/min.

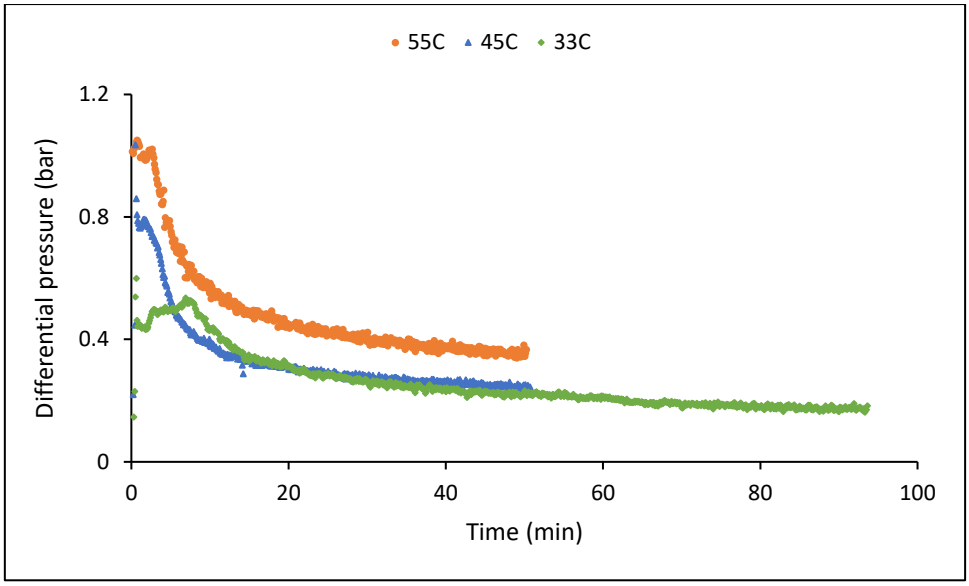

382

383 Figure 7: Effect of temperature on the differential pressure profile of $ScCO_2$-water displacements
384 conducted at 90 bar and 0.4 ml/min.

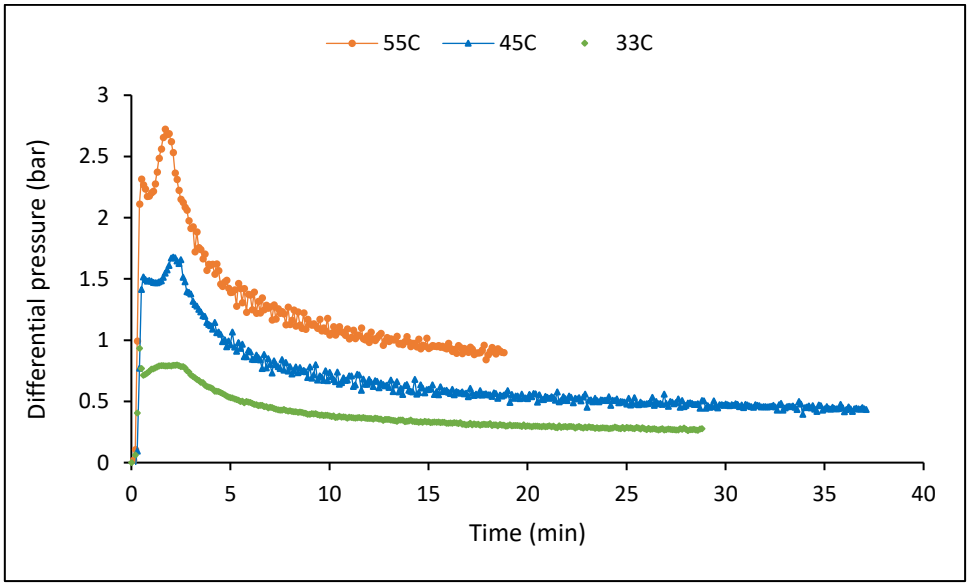

385

386 Figure 8: Effect of temperature on the differential pressure profile of $ScCO_2$-water displacements
387 conducted at 90 bar and 1 ml/min.

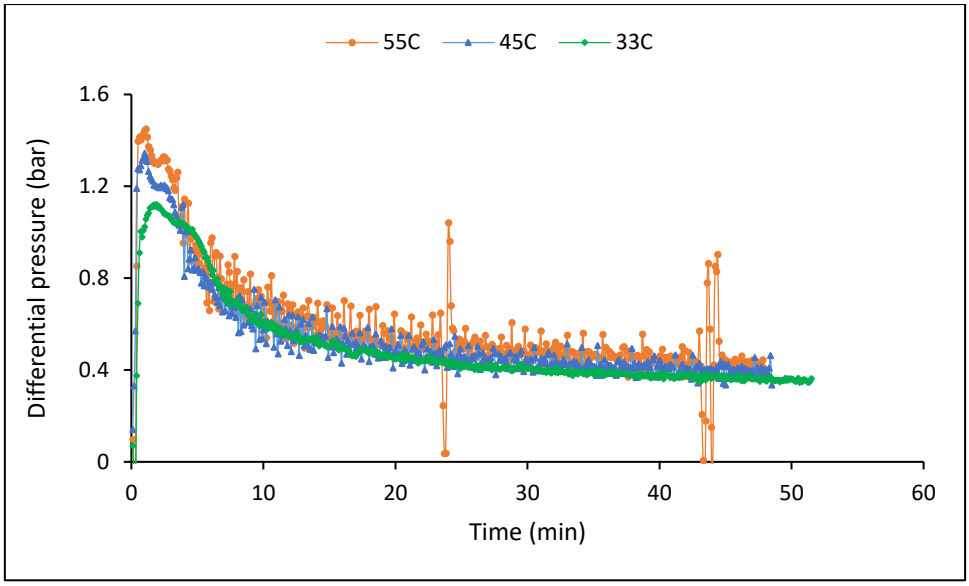

Figure 9: Effect of temperature on the differential pressure profile of $ScCO_2$-water displacements conducted at 75 bar and 0.4 ml/min.

3.1.4 *Effect of Injection Rate on the Differential Pressure Profile of $ScCO_2$-Water Drainage Displacements.*

To investigate the effect of CO_2 injection rate on the differential pressure profile and water recovery of $ScCO_2$-water displacements, three series of experiments were performed under various fluid pressures (74-90 bar), temperatures (33 and 45 °C) and injection rates (0.1, 0.4, and 1ml/min).

Figure 10-12 present the effect of increasing CO_2 injection rate on the differential pressure profile at different conditions. The data show that increasing injection rate caused a considerable increase in the maximum and quasi-differential pressures, the extent of this increase increased with the temperature and reduced with the fluid pressure. The decrease or increase in the corresponding time with increasing injection rate is dependent on the fluid pressure and temperature; the corresponding time decreased at low-temperature (33 °C) and high-fluid pressure (90 bar) conditions but increased at high-temperature (45 °C) and high-fluid pressure (90 bar) conditions. The data show that as the injection rate increased from 0.4 to 1 ml/min: (**I**) the maximum-differential pressure increased by 56% (from 0.599 to 0.935 bar), the quasi-differential pressure was constant, and the corresponding time reduced by 33.33% (from 0.6 to 0.4 min) for the displacements conducted at 90 bar and 33 °C, as shown in Figure 10; (**II**), the maximum-differential pressure increased by around 62% (from 1.035 to 1.674 bar) and the quasi-differential pressure increased by around 85.5% (from 0.234 to 0.434 bar), the

corresponding time increased by 340% (from 0.5 to 2.2 min) for the displacements conducted at 90 bar and 45 °C, as shown in Figure 11; and (**III**) the maximum-differential pressure increased by about 111% (from 1.16 to 2.4446 bar), the quasi-differential pressure by 129% (from around 0.271 to 0.621 bar), and the corresponding time was constant for the displacements conducted at 74 bar and 45 °C, as shown in Figure 12.

According to Eq.1, the increase observed in the differential pressure can be related to the increase in the viscous forces owing to increasing the injection rate; however, the extent of the increase is dependent on the associated fluid pressure and temperature conditions. The reduction in corresponding time at low-temperature and high-pressure conditions can be related to the low maximum-differential pressure because of the transformation of the $ScCO_2$-water displacement behaviour to the likeness of a liquid CO_2-water displacement (Al-Zaidi et al., 2018b); while the increase in the corresponding time at high-temperature and high-pressure conditions can be associated with the high maximum-differential pressure because of the transformation of the $ScCO_2$-water displacement profile to the likeness of a gaseous CO_2-water displacement (Al-Zaidi et al., 2018b).

The data in Figure 11 also show that the increase in the injection rate caused a slight change in the differential pressure profile. After its first reduction, the differential pressure increased for a small period, then continued its reduction until the end of the displacements; the rate of the reduction decreased with time. The increase in the differential pressure profile for a small period means that the injected CO_2 had to open new flow paths after the initial entry. This depends on the core sample properties and operational conditions due to their direct impact on capillary and viscous forces. Moreover, the data from Figure 11 also show that the differential pressure profile of the 0.4 and 0.6 ml/min experiments became nearly identical, during the last period, after around 14 min. This suggests that the effect of pressure drop due to viscous forces became negligible after around 14 min as the majority of water was depleted.

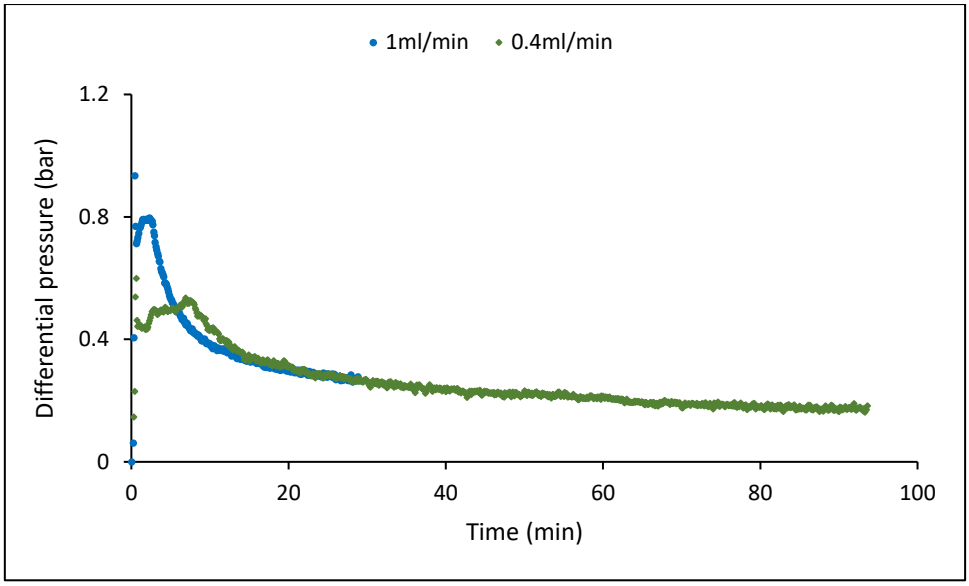

Figure 10: Effect of CO_2 injection rate on the differential pressure profile of $ScCO_2$-water displacements conducted at 90 bar and 33 °C.

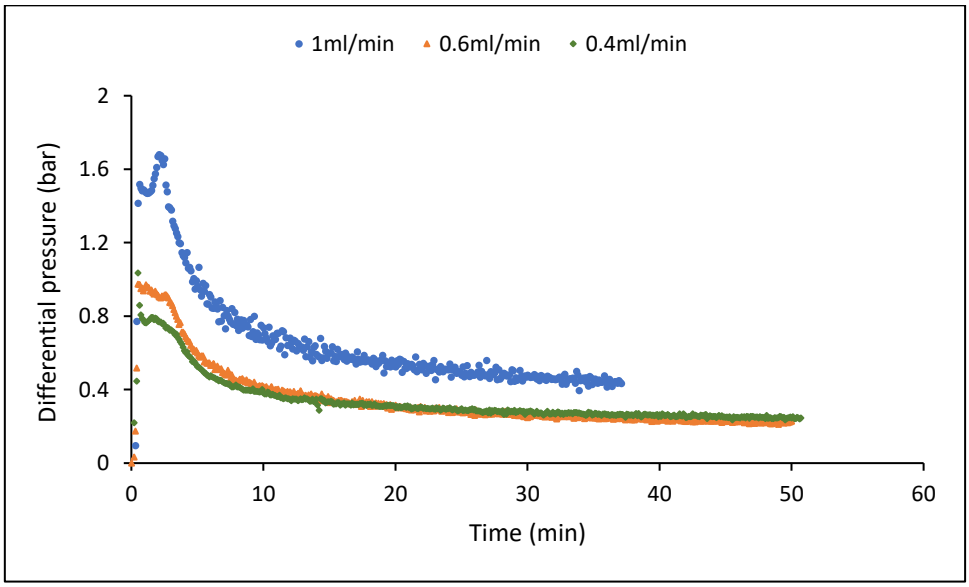

Figure 11: Effect of CO_2 injection rate on the differential pressure profile of $ScCO_2$-water displacements conducted at 90 bar and 45 °C.

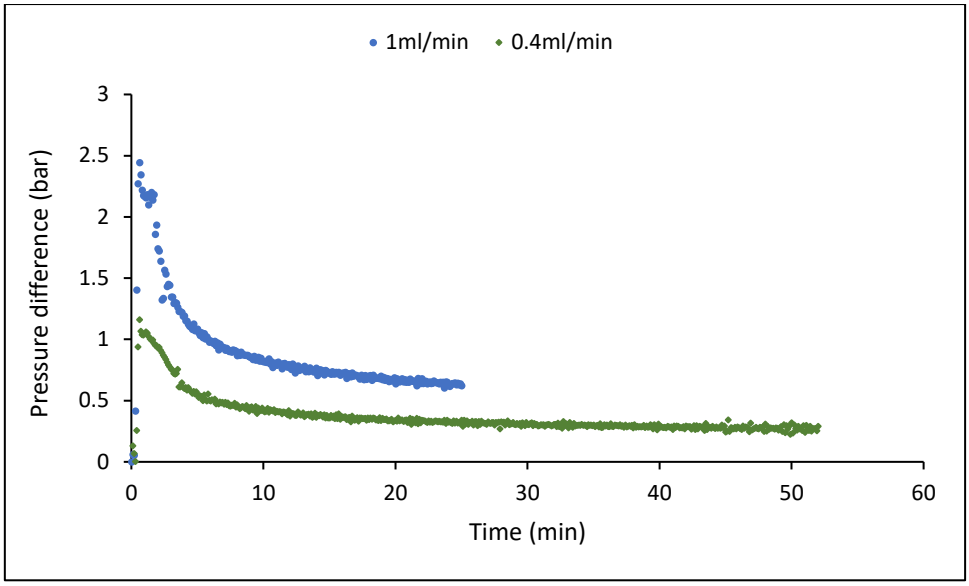

438

439 Figure 12: Effect of CO_2 injection rate on the differential pressure profile of $ScCO_2$-water displacements
440 conducted at 74 bar and 45 °C.

441 In summary, the results show that for all fluid pressures, temperatures and CO_2 injection rates the
442 differential pressure increased sharply; then, it dropped steeply (under low pressures and high
443 temperature conditions) or gradually (under high pressures and low temperature conditions) until it
444 reached an almost quasi-steady status. Increasing fluid pressure caused the differential pressure profile
445 of the $ScCO_2$-water displacements to transform to the likeness of liquid CO_2 behaviour. On contrary,
446 increasing temperature caused it to transform to the likeness of gaseous CO_2 behaviour. Increasing
447 injection rate caused the transition from gaseous to liquid CO_2 behaviour to occur at lower fluid
448 pressures. Increasing fluid pressure caused a slight change in the differential pressure profile; the
449 differential pressure profile of the 90 bar-experiment increased gradually until it became slightly higher
450 than the differential pressure profile of the 80 bar-experiment at the end of the flooding. Increasing
451 temperature at a lower fluid pressure (75 bar) caused the appearance of the differential pressure
452 oscillations. The increase in the injection rate caused a slight change in the differential pressure profile.
453 After its first reduction, the differential pressure increased for a small period, then continued its
454 reduction until the end of the displacements.

455 Increasing fluid pressure caused a substantial drop in the maximum and quasi-differential
456 pressures; the extent of this drop decreased with the injection rate. On the other hand, increasing

457 injection rate and temperature caused a considerable increase in the maximum and quasi-differential
458 pressures; this considerable increase is dependent on the concomitant operational conditions. For
459 increasing temperature, the maximum and quasi-differential pressures increased with the injection
460 rate. For increasing injection rate, the maximum and quasi-differential pressures increased with the
461 temperature and reduced with the fluid pressure. The results indicate that capillary forces have more
462 impact on the differential pressure profiles than viscous forces when fluid pressure and temperature
463 increased but the viscous forces have more impact when injection rate increased significantly.

464 The magnitude of the corresponding time is dependent on many factors such as the operational
465 conditions (e.g. CO_2 injection rate, fluid pressure and temperature) and the core sample and fluids
466 properties. This is because of the direct impact of the above factors on the capillary entry pressure (due
467 to their influence on the CO_2-water interfacial tension and core sample wettability) as well as their direct
468 impact on the density of the injected fluid and the expansion effect. For illustration, a displacement
469 characterized by lower entry pressure, dense CO_2 and high injection rate will reach its maximum-
470 differential pressure faster. Increasing injection rate caused the corresponding time to decrease at low-
471 temperature (33 °C) and high-fluid pressure (90 bar) conditions but increase at high-temperature (45
472 °C) and high-fluid pressure (90 bar) conditions. For increasing fluid pressure and temperature, the
473 decrease or increase in the corresponding time is dependent on the injection rate. For increasing fluid
474 pressure, the corresponding time increased at an injection rate of 0.1 ml/min but decreased at an
475 injection rate of 0.4 ml/min and higher. However, for increasing temperature, the corresponding time
476 decreased at an injection rate of 0.1 ml/min but increased at an injection rate of 0.4 ml/min and higher.

477 *3.2 Water Production Behaviour*

478 This section deals with the impact of fluid pressure, temperature, and CO_2 injection rate on the
479 production behaviour of supercritical CO_2-water displacements.

3.2.1 *Effect of Fluid Pressure on ScCO$_2$-Water Production Behaviour*

Figure 13 shows the effect of increasing fluid pressure on the cumulative produced volumes. The data reveal that increase in fluid pressure led to a reduction in the cumulative produced volumes. As the fluid pressure increased, the difference between the cumulative produced volumes and the cumulative injected volumes decreased. The difference was 1.9, 0.75, 0.38, and -0.363 for the experiments performed at 75, 77, 80, and 90 bar, respectively. The 75 bar-experiment corresponded to the highest difference while the 90 bar-experiment corresponded to the lowest. For the experiments performed at 75, 77, and 80 bar, the cumulative produced volumes were higher than the cumulative injected volumes. As the fluid pressure increased to 90 bar, the cumulative produced volumes became less than the cumulative injected volumes. The high cumulative produced volumes at low pressures mean less volume of CO_2 can be stored at these conditions. However, if the goal is to enhance oil production by reducing the cost of CO_2 then low pressures is a better choice. The increase observed in the cumulative produced volumes can be related mainly to the water production. This is because after about 5 min until the end of the displacements the cumulative produced volumes and the cumulative injected volumes were identical. The similarity between the cumulative injected and produced volumes means that CO_2 volumes cannot cause an increase in the cumulative volumes under our experimental rig configuration. This is because the produced CO_2 shrinks again to its original injected volume after leaving the core sample. Thus, the increase in the cumulative volumes at early stages might reflect the displacement efficiency and the impact of CO_2 expansion.

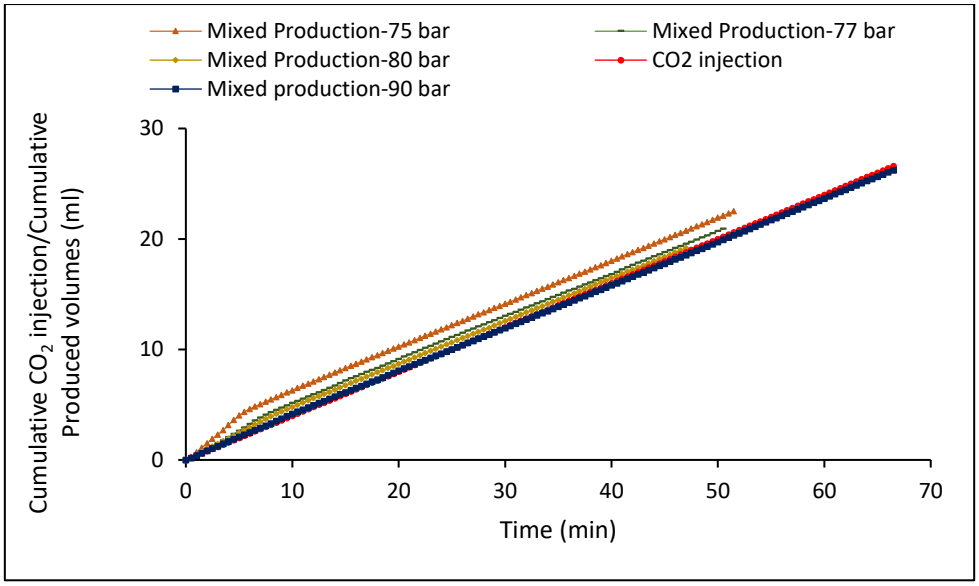

Figure 13: Effect of fluid pressure on the cumulative produced volumes of water and CO_2 of $ScCO_2$-water displacements conducted at 0.4 ml/min, and 33 °C.

3.2.2 *Effect of Temperature on $ScCO_2$-Water Production Behaviour*

The effect of increasing temperature on the cumulative produced volumes is shown in Figure 14. The data reveal that as temperature increased, the cumulative produced volumes increased considerably. As the temperature increased from 33 °C to 55 °C, the cumulative produced volumes increased by around 10.6% (from 20.2 to 22.338 ml). The increase in the cumulative produced volumes can be attributed to the increasing gas expansion and the reducing CO_2 solubility because of increasing temperature (Bachu and Bennion, 2008; Yang et al., 2007). The increase in cumulative produced means less CO_2 can be stored in hot temperature environment.

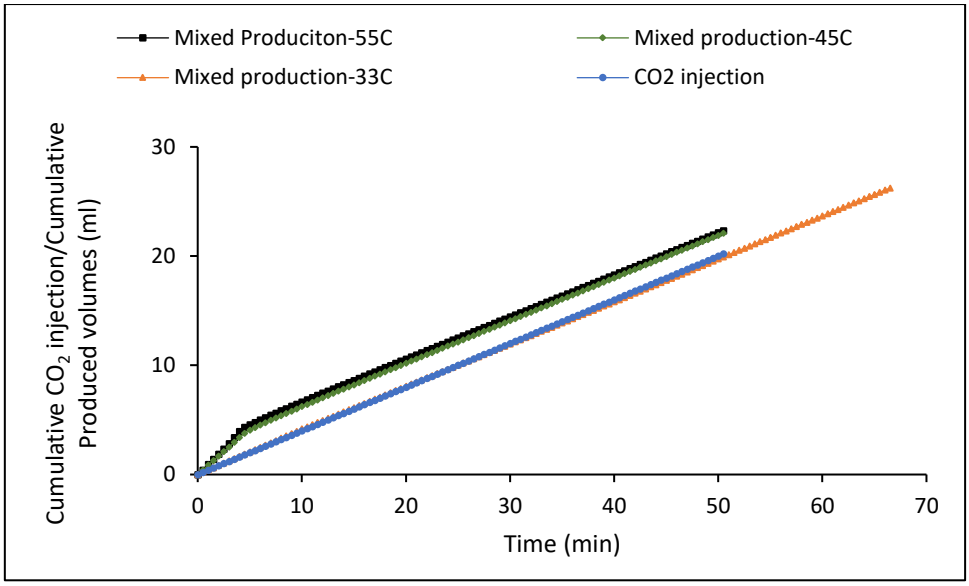

Figure 14: Effect of temperature on the cumulative produced volumes of water and CO_2 of $ScCO_2$-water displacements conducted at 90 bar and 0.4 ml/min.

3.2.3 Effect of Injection Rate on Water Production Behaviour during $ScCO_2$ injection.

Figure 15 shows the effect of increasing injection rate on the cumulative produced volumes. The data from Figure 14 and Figure 15 reveal that as the injection rate increased, from 0.1 to 0.4 ml/min, the cumulative produced volumes increased. The cumulative produced volumes increased by around 9% (from 22.627 to 24.662 ml) at 33 °C and increased by around 2.7% (from 13.711 to 14.078 ml) at 45 °C. The increase in the cumulative volume with increasing injection rate can be related to the increase in water recovery due to the increase in the viscous forces at the expense of capillary forces, which try to reduce production.

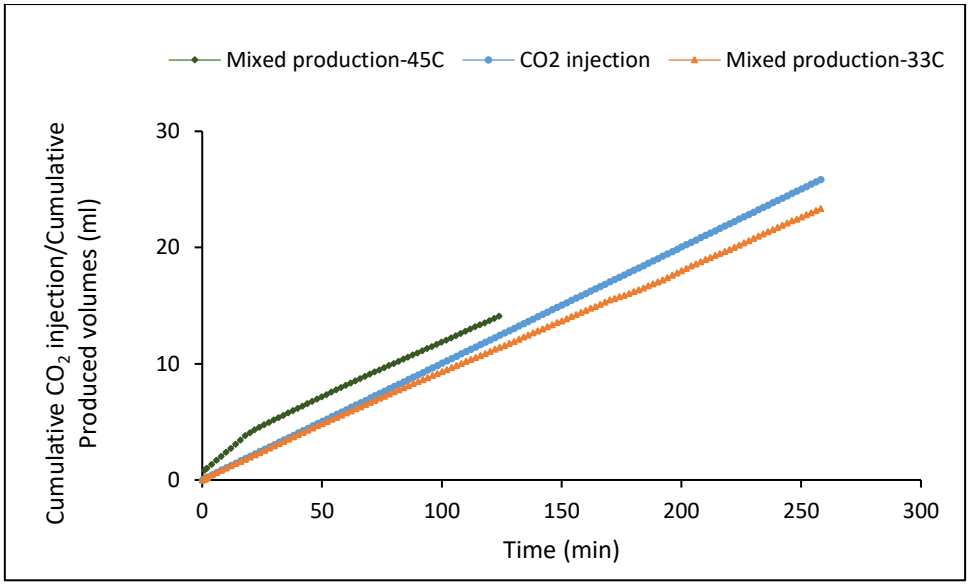

Figure 15: Effect of temperature on the cumulative produced volumes of water and CO_2 of $ScCO_2$-water displacements conducted at 90 bar and 0.1 ml/min.

In summary, the increase in fluid pressure led to a reduction in the cumulative produced volumes while increasing temperature and injection rate caused an increase in them.

3.3 Effect of Fluid Pressure, Temperature, and Injection Rate on Endpoint CO_2 Effective (Relative) Permeability and Residual Water Saturation

The determination of the effective and relative permeability of CO_2 is of practical interest for CO_2 sequestration processes in subsurface formations (Rathnaweera et al., 2015) such as determining the efficiency and integrity of CO_2 storage (Busch and Müller, 2011). At the end of the flooding experiment, the volume of the produced water was measured, and the residual water saturation was calculated using the mass balance concept. Then, the core sample was weighed to confirm the calculated residual water saturation. To calculate the endpoint effective permeability and endpoint relative permeability of supercritical CO_2 using Darcy's law, the average differential pressure and the average CO_2 outflow rate of the last period were used (Akbarabadi and Piri, 2011; Chang et al., 2013). The CO_2 viscosity at the fluid pressure and temperature was calculated using the Peace software website (Peace software, 2017).

Table 1 presents the endpoint effective (K_{fCO2}) and relative permeabilities (K_{rCO2}) of supercritical CO_2 as well as the residual water saturation (S_{wr}) as a function of fluid pressure, temperature, and

injection rate. The results show that both K_{rCO2} (Armstrong et al., 2017) and S_{wr} are dependent on the experimental conditions at which they are measured. The S_{wr} was in range of 0.34 to 0.41 while K_{rCO2} was less than 0.37. Akbarabadi and Piri, as well as, Busch and Müller observed a low relative permeability for CO_2 (Akbarabadi and Piri, 2011; Busch and Müller, 2011), too. Such low relative permeability would tend to decrease injectivity while increasing displacements efficiency (Levine et al., 2011). The results showed a remarkable impact for the parameters investigated on the K_{rCO2} with a lesser impact on the S_{wr}. The data from Table 1 show also that the amount of the injected volumes showed no impact on the S_{wr} trend. Based on the logarithmic values of the viscosity ratio (M) and capillary number (Ca), the invasion pattern of this study is capillary fingering regime, as shown in Figure 16.

In general, increasing fluid pressure led to an increase in the K_{rCO2}. This is in agreement with the findings of Bennion and Bachu (Bennion and Bachu, 2006a). The magnitude of the increase in the K_{rCO2} with increasing fluid pressure depends on the concomitant injection rate and temperature; the endpoint decreased with increasing the injection rate and temperature. The highest increase occurred with low injection rate and low-temperature. As the fluid pressure increased from 75 to 90 bar at 33 °C, the K_{rCO2} increased: (**I**) by about 0.114 for the 0.1 ml/min-displacements, (**II**) by around 0.08 for the 0.4 ml/min-displacements, and (**III**) by approximately 0.07 for the 1 ml/min-displacements. However, as the fluid pressure increased from 75 to 90 bar at 45 °C, the K_{rCO2} increased by about 0.046 for the 0.4 ml/min-displacements. The reduction in the K_{rCO2} as the temperature increased from 33 to 45 °C might be associated with the increase in the capillary forces which hinder the flowrate of the injected CO_2. It should be noted that Liu et al also observed an increase in the K_{rCO2} with increasing fluid pressure (Liu et al., 2010). Bennion and Bachu observed also an increase in the K_{rCO2} and the maximum endpoint CO_2 saturation (i.e. reduction in the Swr) and attributed that to decreasing interfacial tension with increasing pressure (Bennion and Bachu, 2006a).

The results from Table 1 show that in compassion to its impact on K_{rCO2}, the fluid pressure showed a lesser influence on the S_{wr}. Overall, the increase in fluid pressure led to decrease the S_{wr} (Bennion and Bachu, 2006a). Increasing the fluid pressure from 75 to 90 bar at 33 °C resulted in decreasing the S_{wr}: (**I**)

566 by 0.027 for the 0.1 ml/min displacements, (**II**) by 0.015 for the 0.4 ml/min displacements, and (**III**) by
567 0.016 for the 1 ml/min displacements. Increasing the fluid pressure from 75 to 90 bar at 45 °C and 0.4
568 ml/min produced a reduction in the S_{wr} by 0.025. The main reasons behind the reduction in the S_{wr} are
569 the increase in the *Ca* and the reduction in the *M* as illustrated in Table 1. It should be noted that the
570 displacement conducted at 80 bar-0.1 ml/min-33 °C showed the lowest S_{wr} of 0.343 and the highest K_{rCO2}
571 of around 0.223, the reason is not entirely clear. However, this might be related to the transition from
572 the likeness of gaseous to liquid CO_2 behaviour as the fluid pressure increased from 75 to 80 and then
573 to 90 bar, as shown in Figure 1.

574 The results from Table 1 reveal that the impact of the temperature on the K_{rCO2} depends largely on
575 the associated fluid pressure and injection rate. The K_{rCO2} showed a declining trend with increasing
576 temperature at high-fluid pressures (90 bar) but an increasing trend at lower-fluid pressures (75 bar).
577 With increasing fluid temperature, the percentage of the reduction in the K_{rCO2} at high-fluid pressures
578 increased with the injection rate. For the 90 bar-core floodings, increasing temperature from 33 to 45 °C
579 at low injection rate (0.1ml/min) caused the K_{rCO2} to decrease by around 0.081. As the temperature
580 increased from 33 to 55 °C, the K_{rCO2} dropped by about 0.121 for the 0.4ml/min-displacements, and by
581 0.239 for the 1 ml/min-displacements. On the other hand, for the 75 bar-core floodings, as the
582 temperature increased from 33 to 55 °C, the K_{rCO2} increased slightly by around 0.015; the reason is not
583 clear. However, it might be also associated with the slight increase in pressure drop despite the high
584 reduction in CO_2 viscosity with increasing temperature; the slight increase in pressure drop might be
585 associated with the transfer of supercritical CO_2 behaviour towards gaseous CO_2 behaviour, especially
586 under high-temperature and low-fluid pressure conditions, as shown in Figure 9. It should be noted
587 that there is no consensus in the literature about the effect of temperature on the relative permeability.
588 For illustration, Bennion and Bachu (Bennion and Bachu, 2006b) observed a reduction in the relative
589 permeability with increasing temperature. On the other hand, Lee et al. observed almost no change in
590 the relative permeability with increasing temperature (Lee et al., 2009).

591 Generally, the results from Table 1 reveal that the increase in temperature led to an increase in the
592 S_{wr}. The magnitude of the increase depends on the associated fluid pressure and injection rate. Overall,
593 as the temperature increased, the increase in the S_{wr} increased with the injection rate and fluid pressure.
594 As the temperature increased from 33 to 45 °C, the S_{wr} increased by 0.004 for the experiments conducted
595 at 90 bar and 0.1 ml/min. When the temperature increased from 33 to 55 °C, the S_{wr} increased by 0.021
596 for the experiments conducted at 90 bar and 0.4 ml/min, by 0.041 for the experiments conducted at 90
597 bar and 1 ml/min, and by 0.018 for the experiments conducted at 75 bar and 0.4 ml/min and. Overall,
598 the reduction in the K_{rCO2} and the increase in S_{wr} can be related to the reduction in the *Ca* and the increase
599 in the *M*.

600 In general, the results from Table 1 reveal that the increase in the CO_2 injection rate caused a rise
601 in the K_{rCO2} and a reduction in the S_{wr}. These findings agree qualitatively with those obtained by Chang
602 et al. and Akbarabadi and Piri (Akbarabadi and Piri, 2011; Chang et al., 2013). As the injection rate
603 increased, the change in the K_{rCO2} and S_{wr} increased with the fluid pressure but decreased with the
604 temperature. Overall, as the injection rate increased from 0.1 to 1 ml/min, the K_{rCO2} increased by about
605 0.038 for the 75 bar-33 °C-core floodings, by around 0.134 for the 90 bar-33 °C-core floodings, by about
606 1.68 for the 74 bar-45 °C-core floodings, and by 0.084 for the 90 bar-45 °C-core floodings. The S_{wr}
607 decreased by 0.033, 0.034, 0.006, and 0.012 for the above experiments, respectively. Since M is constant,
608 the reduction in the S_{wr} can be related mainly to the increase observed in the Ca. On the other hand, the
609 displacements conducted at 80 bar showed an opposite behaviour. As the injection rate increased from
610 0.1 to 1ml/min, the K_{rCO2} decreased by 0.08 and the S_{wr} increased by 0.041. The reason is not entirely
611 clear. However, this might be related to the transition of supercritical CO_2 behaviour from gaseous to
612 liquid-like CO_2 behaviour as the fluid pressure increased from 75 to 80 and then to 90 bar, see Figure 1.

613

614

615 Table 1: Effect of fluid pressure, temperature, and injection rate on the endpoint effective permeability
616 (K_{fCO2}), endpoint relative permeability (K_{rCO2}) and residual water saturation (S_{wr}).

Parameter	*Experiment*	K_{fCO2} *(mD)*	K_{rCO2}	S_{wr}	*Ca*	*M*	*Injected* CO_2 *(ml)*
Fluid Pressure Effect	75 bar-0.1 ml/min-33 °C	1.095	0.06982	0.411	6.417E-08	22.47	20.19
	80 bar-0.1ml/min-33°C	3.495	0.22287	0.343	6.613E-08	16.31	24.7
	90 bar-0.1ml/min-33°C	2.880	0.18370	0.384	7.413E-08	13.91	25.82
	75 bar-0.4ml/min-33°C	1.858	0.11849	0.372	2.566E-07	22.47	20.6
	77 bar-0.4ml/min-33°C	2.207	0.14077	0.374	2.594E-07	19.53	19.84
	80 bar-0.4ml/min-33°C	2.388	0.15228	0.372	2.645E-07	16.31	18.36
	90 bar-0.4ml/min-33°C	3.128	0.19949	0.357	2.965E-07	13.91	37.36
	75 bar-1ml/min-33°C	1.696	0.10818	0.366	6.417E-07	22.47	20
	80 bar-1ml/min-33°C	2.307	0.14715	0.362	6.613E-07	16.31	20.5
	90 bar-1ml/min-33°C	2.815	0.17951	0.35	7.413E-07	13.91	20.3
	75 bar-0.4ml/min-45°C	1.897	0.12099	0.39	2.577E-07	29.59	19.52
	80 bar-0.4ml/min-45°C	2.714	0.17306	0.363	2.497E-07	27.93	19.24
	90 bar-0.4ml/min-45°C	2.619	0.16701	0.365	2.467E-07	20.62	20.04
Temperature Effect	90 bar-0.1ml/min-33°C	3.677	0.23451	0.384	7.413E-08	13.91	25.82
	90 bar-0.1ml/min-45°C	2.404	0.15330	0.388	6.168E-08	20.62	25.14
	90 bar-0.4ml/min-33°C	4.019	25.632	0.357	2.965E-07	13.91	37.36
	90 bar-0.4ml/min-45°C	2.629	0.16769	0.365	2.467E-07	20.62	20
	90 bar-0.4ml/min-55°C	2.123	0.13538	0.378	2.445E-07	22.73	20.08
	90 bar-1ml/min-33°C	5.780	0.36862	0.35	7.413E-07	13.91	20.3
	90 bar-1ml/min-45°C	2.918	0.18607	0.374	6.168E-07	20.62	36.7
	90 bar-1ml/min-55°C	2.032	0.12.960	0.391	6.114E-07	22.73	18.8
	75 bar-0.4ml/min-33°C	1.921	0.12254	0.372	2.566E-07	22.47	20.6
	75 bar-0.4ml/min-45°C	1.995	0.12722	0.39	2.577E-07	29.59	19.4
	75 bar-0.4ml/min-55°C	2.160	0.13777	0.39	2.641E-07	25.91	19.16
Injection Rate Effect	75 bar-0.1ml/min-33°C	1.095	0.06982	0.411	6.417E-08	22.47	20.19
	75 bar-0.4ml/min-33°C	1.921	0.12254	0.372	2.566E-07	22.47	20.6
	75 bar-1ml/min-33°C	1.696	0.10818	0.378	6.417E-07	22.47	20
	90 bar-0.1ml/min-33°C	3.677	0.23451	0.384	7.41E-08	13.91	25.82

90 bar-0.2ml/min-33°C	1.755	0.1119	0.386	1.48E-07	13.91	17.24
90 bar-0.4ml/min-33°C	4.019	0.25632	0.357	2.97E-07	13.91	37.36
90 bar-1ml/min-33°C	5.78	0.36862	0.35	7.41E-07	13.91	20.3
74 bar-0.4ml/min-45°C	2.902	0.18508	0.39	2.60E-07	29.94	25
74 bar-1ml/min-45°C	3.166	0.20192	0.384	6.50E-07	29.94	20.56
90 bar-0.1ml/min-45°C	2.404	0.1533	0.368	6.17E-08	20.62	25.14
90 bar-0.4ml/min-45°C	2.629	0.16769	0.365	2.47E-07	20.62	19.76
90 bar-0.6ml/min-45°C	4.333	0.27636	0.353	3.70E-07	20.62	29.63
90 bar-1ml/min-45°C	3.711	0.23666	0.356	6.17E-07	20.62	37.1
80 bar-0.1ml/min-33°C	3.569	0.22761	0.343	6.613E-08	16.31	24.7
80 bar-0.4ml/min-33°C	2.388	0.15228	0.372	2.645E-07	16.31	18.36
80 bar-1ml/min-33°C	2.307	0.14715	0.384	6.613E-07	16.31	20.5

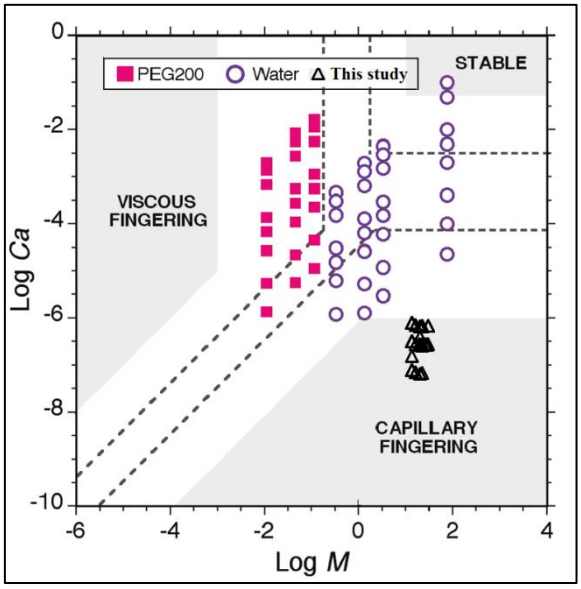

Figure 16: Stability diagram showing three flow regimes and the locations of the PEG200, water displacement, and the data of this study. The dashed lines indicate the flow regimes according to Zhang et al., and the shaded areas indicate flow regimes according to Lenormand et al. (Lenormand et al., 1988; Zhang et al., 2011).

4 Conclusion

This study investigated the impact of fluid pressure, temperature, and CO_2 injection rate on the dynamic pressure evolution, displacement efficiency, and endpoint CO_2 effective (relative) permeability during the injection of supercritical CO_2 into a water-saturated sandstone core sample. The experiments highlight the importance of the balance between capillary and viscous forces on the

627 pressure and production data. The results reveal that the extent of the impact of each parameter (e.g.
628 fluid pressure) on the pressure and production profiles is a function of the associated parameters (e.g.
629 temperature and injection rate). The results indicate that capillary forces dominate the multiphase flow
630 characteristics as fluid pressure and temperature are increased.
631
632 Importantly, the results demonstrate that increasing fluid pressure caused a considerable reduction in
633 the differential pressure and a transformation of the profile of the $ScCO_2$-water displacements to be
634 similar to that of liquid CO_2-water displacements; while, increasing temperature resulted in a
635 significant increase in the differential pressure profile and a transition towards that of gaseous CO_2-
636 water displacements. Increasing the injection rate caused the transformation to occur at lower
637 pressures, and led to a substantial increase in the differential pressure; the extent of this increase
638 increased with increasing temperature and reduced with increasing fluid pressure. The changes
639 observed in the differential pressure with varying fluid pressure and temperature reflect a change in
640 the influence of the capillary forces. The change in the capillary forces will have a direct impact on the
641 displacement efficiency and the entry pressure. For illustration, the reduction in the capillary forces
642 with increasing fluid pressure will reduce the entry pressure; thereby, it will have a reduction impact
643 on the storage capacity and sealing efficiency of the target formation by enhancing the upward
644 migration of CO_2. The reduction observed in the differential pressure as CO_2 transformed to a liquid-
645 like behaviour means less energy is required for the displacement of fluids in host formations, which
646 can reduce the cost of production significantly.
647
648 Also, of particular importance is that increasing temperature at a lower fluid pressure (75 bar) caused
649 the appearance of the differential pressure oscillations. The appearance of the oscillations can increase
650 CO_2 residual saturation due to the re-imbibition process accompanied with these oscillations, thereby
651 increasing the storage capacity and integrity of CO_2. The differential pressure required to open the

652 blocked flow channels during these oscillations can be useful in calculating the largest effective pore
653 diameters and hence the sealing efficiency of the rock.
654
655 The time required to reach the maximum differential pressure, i.e. the corresponding time, is dependent
656 on fluid pressure, temperature, and injection rate. The change in the corresponding time might give an
657 indication whether the change in the operational conditions can hasten or delay the time of CO_2
658 breakthrough out of the system.
659
660 The increase in fluid pressure led to a reduction in the cumulative produced volumes. On the other
661 hand, increasing temperature and injection rate caused an increase in the cumulative produced
662 volumes.
663
664 The results show that both endpoint relative CO_2 permeability (K_{rCO2}) and residual water saturation
665 (S_{wr}) are dependent on the experimental conditions at which they are measured. The S_{wr} was in range
666 of 0.34 -0.41 while K_{rCO2} was less than 0.37. Increasing pressure and injection rate caused an increase in
667 K_{rCO2} and a reduction in S_{wr}. K_{rCO2} showed a declining trend with increasing temperature at high fluid
668 pressures (90 bar) but an increasing trend at lower fluid pressures (75 bar). S_{wr} increased as temperature
669 increased.

670 **Acknowledgements**: The authors wish to thank the Higher Committee for Education
671 Development in Iraq and the Ministry of Oil in Iraq for their sponsorship of the first author PhD study.

672 ## Reference

673 Aggelopoulos, C., Robin, M., Perfetti, E., Vizika, O., 2010. CO2/CaCl2 solution interfacial tensions
674 under CO2 geological storage conditions: influence of cation valence on interfacial tension. Advances
675 in Water Resources 33, 691-697.
676 Akbarabadi, M., Piri, M., 2011. Geologic storage of carbon dioxide: an experimental study of
677 permanent capillary trapping and relative permeability, In Proceedings of International Symposium
678 of the Society of Core Analysts, Austin, Texas, USA. 18–21 September 2011, pp. 18-21.

679 Akbarabadi, M., Piri, M., 2013. Relative permeability hysteresis and capillary trapping characteristics
680 of supercritical CO2/brine systems: An experimental study at reservoir conditions. Advances in Water
681 Resources 52, 190-206.
682 Al-Menhali, A., Krevor, S., 2014. Effective wettability measurements of CO2-brine-sandstone system
683 at different reservoir conditions. Energy Procedia 63, 5420-5426.
684 Al-Zaidi, E., Fan, X., Edlmann, K., 2018a. The Effect of CO2 Phase on Oil Displacement in a Sandstone
685 Core Sample. Fluids 3, 23.
686 Al-Zaidi, E., Nash, J., Fan, X., 2018b. Effect of CO2 phase on its water displacements in a sandstone
687 core sample. International Journal of Greenhouse Gas Control 71, 227-238.
688 Alemu, B.L., Aker, E., Soldal, M., Johnsen, Ø., Aagaard, P., 2011. Influence of CO2 on rock physics
689 properties in typical reservoir rock: a CO2 flooding experiment of brine saturated sandstone in a CT-
690 scanner. Energy Procedia 4, 4379-4386.
691 Alkan, H., Cinar, Y., Ülker, E., 2010. Impact of capillary pressure, salinity and in situ conditions on
692 CO2 injection into saline aquifers. Transport in porous media 84, 799-819.
693 Armstrong, R.T., McClure, J., Berill, M., Rücker, M., Schlüter, S., Berg, S., 2017. Flow Regimes During
694 Immiscible Displacement. Petrophysics 58, 10-18.
695 Aryana, S.A., Kovscek, A.R., 2012. Experiments and analysis of drainage displacement processes
696 relevant to carbon dioxide injection. Physical Review E 86.
697 Bachu, S., 2000. Sequestration of CO2 in geological media: criteria and approach for site selection in
698 response to climate change. Energy conversion and management 41, 953-970.
699 Bachu, S., 2001. Geological sequestration of anthropogenic carbon dioxide: applicability and current
700 issues. Geological perspectives of global climate change, 285-303.
701 Bachu, S., Bennion, D.B., 2008. Interfacial tension between CO2, freshwater, and brine in the range of
702 pressure from (2 to 27) MPa, temperature from (20 to 125)° C, and water salinity from (0 to 334 000)
703 mg· L− 1. Journal of Chemical & Engineering Data 54, 765-775.
704 Bachu, S., Bennion, D.B., 2009. Dependence of CO2-brine interfacial tension on aquifer pressure,
705 temperature and water salinity. Energy Procedia 1, 3157-3164.
706 Bahralolom, I., Bretz, R., Orr Jr, F., 1988. Experimental investigation of the interaction of phase
707 behavior with microscopic heterogeneity in a CO2 flood. SPE reservoir engineering 3, 662-672.
708 Basbug, B., Gumrah, F., Oz, B., 2005. Simulating the Effects of Deep Saline Aquifer Properties on CO2
709 Sequestration, Canadian International Petroleum Conference. Petroleum Society of Canada.
710 Bennion, D.B., Bachu, S., 2006a. Dependence on temperature, pressure, and salinity of the IFT and
711 relative permeability displacement characteristics of CO2 injected in deep saline aquifers, SPE Annual
712 Technical Conference and Exhibition. Society of Petroleum Engineers.
713 Bennion, D.B., Bachu, S., 2006b. The impact of interfacial tension and pore size distribution/capillary
714 pressure character on CO2 relative permeability at reservoir conditions in CO2-brine systems, In
715 Proceedings of the SPE/DOE Symposium on Improved Oil Recovery. Society of Petroleum Engineers:
716 Houston, TX, USA, 2006., Tulsa, OK, USA, 22–26 April 2006.
717 Berg, S., Oedai, S., Ott, H., 2013. Displacement and mass transfer between saturated and unsaturated
718 CO2–brine systems in sandstone. International Journal of Greenhouse Gas Control 12, 478-492.
719 Bikkina, P., Wan, J., Kim, Y., Kneafsey, T.J., Tokunaga, T.K., 2016. Influence of wettability and
720 permeability heterogeneity on miscible CO2 flooding efficiency. Fuel 166, 219-226.
721 Bikkina, P.K., 2011. Contact angle measurements of CO2–water–quartz/calcite systems in the
722 perspective of carbon sequestration. International Journal of Greenhouse Gas Control 5, 1259-1271.
723 Busch, A., Müller, N., 2011. Determining CO2/brine relative permeability and capillary threshold
724 pressures for reservoir rocks and caprocks: Recommendations for development of standard
725 laboratory protocols. Energy Procedia 4, 6053-6060.
726 Cao, S.C., Dai, S., Jung, J., 2016. Supercritical CO2 and brine displacement in geological carbon
727 sequestration: Micromodel and pore network simulation studies. International Journal of Greenhouse
728 Gas Control 44, 104-114.

729 Carpenter, C., 2014. Enhanced Recovery in Unconventional Liquid Reservoirs by Use of CO2. SPE-
730 0714-0138-JPT 66, 138–141.
731 Chang, C., Zhou, Q., Xia, L., Li, X., Yu, Q., 2013. Dynamic displacement and non-equilibrium
732 dissolution of supercritical CO2 in low-permeability sandstone: An experimental study. International
733 Journal of Greenhouse Gas Control 14, 1-14.
734 Chatzis, I., Morrow, N.R., 1984. Correlation of capillary number relationships for sandstone. Society
735 of Petroleum Engineers Journal 24, 555-562.
736 Chiquet, P., Daridon, J.-L., Broseta, D., Thibeau, S., 2007. CO2/water interfacial tensions under
737 pressure and temperature conditions of CO2 geological storage. Energy Conversion and Management
738 48, 736-744.
739 Delshad, M., Wheeler, M.F., Kong, X., 2010. A critical assessment of CO2 injection strategies in saline
740 aquifers, SPE Western Regional Meeting. Society of Petroleum Engineers.
741 Edlmann, K., Haszeldine, S., McDermott, C., 2013. Experimental investigation into the sealing
742 capability of naturally fractured shale caprocks to supercritical carbon dioxide flow. Environmental
743 earth sciences 70, 3393-3409.
744 Espinoza, D.N., Santamarina, J.C., 2010. Water-CO2-mineral systems: Interfacial tension, contact
745 angle, and diffusion—Implications to CO2 geological storage. Water resources research 46.
746 Farokhpoor, R., Bjørkvik, B.J., Lindeberg, E., Torsæter, O., 2013a. CO2 Wettability Behavior During
747 CO2 Sequestration in Saline Aquifer-An Experimental Study on Minerals Representing Sandstone
748 and Carbonate. Energy Procedia 37, 5339-5351.
749 Farokhpoor, R., Bjørkvik, B.J.A., Lindeberg, E., Torsæter, O., 2013b. Wettability behaviour of CO2 at
750 storage conditions. International Journal of Greenhouse Gas Control 12, 18-25.
751 Fulcher Jr, R.A., Ertekin, T., Stahl, C., 1985. Effect of capillary number and its constituents on two-
752 phase relative permeability curves. Journal of Petroleum Technology 37, 249-260.
753 Gozalpour, F., Ren, S., Tohidi, B., 2005. CO2 EOR and storage in oil reservoir. Oil & gas science and
754 technology 60, 537-546.
755 Hangx, S., van der Linden, A., Marcelis, F., Bauer, A., 2013. The effect of CO2 on the mechanical
756 properties of the captain sandstone: geological storage of CO2 at the Goldeneye field (UK).
757 International Journal of Greenhouse Gas Control 19, 609-619.
758 Herring, A.L., Andersson, L., Newell, D., Carey, J., Wildenschild, D., 2014. Pore-scale observations of
759 supercritical CO2 drainage in Bentheimer sandstone by synchrotron x-ray imaging. International
760 Journal of Greenhouse Gas Control 25, 93-101.
761 Hildenbrand, A., Schlömer, S., Krooss, B., 2002. Gas breakthrough experiments on fine-grained
762 sedimentary rocks. Geofluids 2, 3-23.
763 Jobard, E., Sterpenich, J., Pironon, J., Corvisier, J., Jouanny, M., Randi, A., 2013. Experimental
764 simulation of the impact of a thermal gradient during geological sequestration of CO2: The
765 COTAGES experiment. International Journal of Greenhouse Gas Control 12, 56-71.
766 Jung, J.-W., Wan, J., 2012. Supercritical CO2 and ionic strength effects on wettability of silica surfaces:
767 Equilibrium contact angle measurements. Energy & Fuels 26, 6053-6059.
768 Kaveh, N.S., Wolf, K., Ashrafizadeh, S., Rudolph, E., 2012. Effect of coal petrology and pressure on
769 wetting properties of wet coal for CO2 and flue gas storage. International Journal of Greenhouse Gas
770 Control 11, S91-S101.
771 Kazemifar, F., Blois, G., Kyritsis, D.C., Christensen, K.T., 2015. Quantifying the flow dynamics of
772 supercritical CO2–water displacement in a 2D porous micromodel using fluorescent microscopy and
773 microscopic PIV. Advances in Water Resources.
774 Krevor, S., Pini, R., Benson, S.M., 2013. Measurement of the multiphase flow properties of the CO2
775 brine system for carbon sequestration. Energy Procedia 37, 4499-4503.
776 Kwelle, S.O., 2017. Experimental studies on resistance to fluid displacement in single pores, School of
777 Engineering, Institute of Material and Process. The University of Edinburgh, Edinburgh, UK, p. 206.

778 Lee, Y., Kim, K., Lee, T., Sung, W., Park, Y., Lee, J., 2009. Analysis of CO2 endpoint relative
779 permeability and injectivity by change in pressure, temperature, and phase in saline aquifer. Energy
780 Sources, Part A: Recovery, Utilization, and Environmental Effects 32, 83-99.
781 Lenormand, R., Touboul, E., Zarcone, C., 1988. Numerical models and experiments on immiscible
782 displacements in porous media. Journal of Fluid Mechanics 189, 37-38.
783 Levine, J.S., Matter, J.M., Goldberg, D.S., Lackner, K.S., Supp, M.G., Ramakrishnan, T., 2011. Two
784 phase brine-CO2 flow experiments in synthetic and natural media. Energy Procedia 4, 4347-4353.
785 Li, X., 2015. Experimental Studies on Pore Wetting and Displacement of Fluid by CO2 in Porous
786 Media. University of Edinburgh, Edinburgh, UK.
787 Li, X., Boek, E., Maitland, G.C., Trusler, J.P.M., 2012. Interfacial Tension of (Brines + CO2): (0.864 NaCl
788 + 0.136 KCl) at Temperatures between (298 and 448) K, Pressures between (2 and 50) MPa, and Total
789 Molalities of (1 to 5) mol·kg–1. Journal of Chemical & Engineering Data 57, 1078-1088.
790 Liu, N., Ghorpade, S.V., Harris, L., Li, L., Grigg, R.B., Lee, R.L., 2010. The effect of pressure and
791 temperature on brine-CO2 relative permeability and IFT at reservoir conditions, In Proceedings of
792 theSPE Eastern Regional Meeting. Society of Petroleum Engineers: Houston, TX, USA, 2010.,
793 Morgantown, WV, USA, 13–15 October 2010.
794 Ma, J., Petrilli, D., Manceau, J.-C., Xu, R., Audigane, P., Shu, L., Jiang, P., Le-Nindre, Y.M., 2013. Core
795 scale modelling of CO2 flowing: identifying key parameters and experiment fitting. Energy Procedia
796 37, 5464-5472.
797 Mijic, A., LaForce, T.C., Muggeridge, A.H., 2014. CO2 injectivity in saline aquifers: The impact of non-
798 Darcy flow, phase miscibility, and gas compressibility. Water Resources Research 50, 4163-4185.
799 Müller, N., 2011. Supercritical CO2-brine relative permeability experiments in reservoir rocks—
800 Literature review and recommendations. Transport in porous media 87, 367-383.
801 Nutt, C., 1982. The physical basis of the displacement of oil from porous media by other fluids: a
802 capillary bundle model, Proceedings of the Royal Society of London A: Mathematical, Physical and
803 Engineering Sciences. The Royal Society, pp. 155-178.
804 Ott, H., de Kloe, K., Marcelis, F., Makurat, A., 2011. Injection of supercritical CO2 in brine saturated
805 sandstone: pattern formation during salt precipitation. Energy Procedia 4, 4425-4432.
806 Ott, H., Pentland, C., Oedai, S., 2015. CO2–brine displacement in heterogeneous carbonates.
807 International Journal of Greenhouse Gas Control 33, 135-144.
808 Peace software, 2017.
809 Pentland, C., El-Maghraby, R., Georgiadis, A., Iglauer, S., Blunt, M., 2011. Immiscible displacements
810 and capillary trapping in CO2 storage. Energy Procedia 4, 4969-4976.
811 Perrin, J.-C., Benson, S., 2010. An experimental study on the influence of sub-core scale
812 heterogeneities on CO2 distribution in reservoir rocks. Transport in porous media 82, 93-109.
813 Pini, R., Krevor, S.C., Benson, S.M., 2012. Capillary pressure and heterogeneity for the CO2/water
814 system in sandstone rocks at reservoir conditions. Advances in Water Resources 38, 48-59.
815 Plug, W.-J., Bruining, J., 2007a. Capillary pressure for the sand–CO2–water system under various
816 pressure conditions. Application to CO2 sequestration. Advances in Water Resources 30, 2339-2353.
817 Plug, W.-J., Bruining, J., 2007b. Capillary pressure for the sand–CO 2–water system under various
818 pressure conditions. Application to CO 2 sequestration. Advances in Water Resources 30, 2339-2353.
819 Rathnaweera, T., Ranjith, P., Perera, M., 2015. Effect of salinity on effective CO2 permeability in
820 reservoir rock determined by pressure transient methods: An experimental study on Hawkesbury
821 sandstone. Rock Mechanics and Rock Engineering 48, 2093-2110.
822 Rezaei, N., Firoozabadi, A., 2014. Pressure evolution and production performance of waterflooding in
823 n-heptane-saturated fired berea cores. SPE Journal 19, 674-686.
824 Roof, J., 1970. Snap-off of oil droplets in water-wet pores. Society of Petroleum Engineers Journal 10,
825 85-90.
826 Rostami, B., Kharrat, R., Ghotbi, C., Tabatabaie, S., 2010. Gas-oil relative permeability and residual oil
827 saturation as related to displacement instability and dimensionless numbers. Oil & Gas Science and
828 Technology–Revue de l'Institut Français du Pétrole 65, 299-313.

Saeedi, A., Rezaee, R., Evans, B., Clennell, B., 2011. Multiphase flow behaviour during CO2 geo-sequestration: Emphasis on the effect of cyclic CO2–brine flooding. Journal of Petroleum Science and Engineering 79, 65-85.
Sakurovs, R., Lavrencic, S., 2011. Contact angles in CO2-water-coal systems at elevated pressures. International Journal of Coal Geology 87, 26-32.
Saraji, S., Goual, L., Piri, M., Plancher, H., 2013. Wettability of supercritical carbon dioxide/water/quartz systems: simultaneous measurement of contact angle and interfacial tension at reservoir conditions. Langmuir : the ACS journal of surfaces and colloids 29, 6856-6866.
Schembre, J.M., Kovscek, A.R., 2003. A technique for measuring two-phase relative permeability in porous media via X-ray CT measurements. Journal of Petroleum Science and Engineering 39, 159-174.
Shi, J.-Q., Xue, Z., Durucan, S., 2011. Supercritical CO2 core flooding and imbibition in Tako sandstone—Influence of sub-core scale heterogeneity. International Journal of Greenhouse Gas Control 5, 75-87.
Song, Y., Jiang, L., Liu, Y., Yang, M., Zhao, Y., Zhu, N., Dou, B., Abudula, A., 2012. An experimental study on CO2/water displacement in porous media using high-resolution magnetic resonance imaging. International Journal of Greenhouse Gas Control 10, 501-509.
Suekane, T., Soukawa, S., Iwatani, S., Tsushima, S., Hirai, S., 2005. Behavior of supercritical CO2 injected into porous media containing water. Energy 30, 2370-2382.
Suenaga, H., Nakagawa, K., 2011. Analysis of two-phase flow properties of sandstones to evaluate their suitability for geologic storage of CO2. Energy Procedia 4, 4323-4330.
Tutolo, B.M., Luhmann, A.J., Kong, X.-Z., Saar, M.O., Seyfried, W.E., 2015. CO2 sequestration in feldspar-rich sandstone: coupled evolution of fluid chemistry, mineral reaction rates, and hydrogeochemical properties. Geochimica et Cosmochimica Acta 160, 132-154.
Wang, D., Dong, B., Breen, S., Zhao, M., Qiao, J., Liu, Y., Zhang, Y., Song, Y., 2015. Review: Approaches to research on CO2/brine two-phase migration in saline aquifers. Hydrogeology Journal 23, 1-18.
Wang, D., Zhao, M., Song, Y., Xu, H., Ma, X., 2013. Influence of Capillary Pressure and Injection Rate as well as Heterogeneous and Anisotropic Permeability on CO2 Transport and Displacement Efficiency in Water-Saturated Porous Media. Energy Procedia 37, 3945-3951.
Xu, R., Luo, S., Jiang, P., 2011. Pore scale numerical simulation of supercritical CO2 injecting into porous media containing water. Energy Procedia 4, 4418-4424.
Yang, D., Gu, Y., Tontiwachwuthikul, P., 2007. Wettability determination of the reservoir brine−reservoir rock system with dissolution of CO2 at high pressures and elevated temperatures. Energy & Fuels 22, 504-509.
Yang, D., Tontiwachwuthikul, P., Gu, Y., 2005. Interfacial interactions between reservoir brine and CO2 at high pressures and elevated temperatures. Energy & Fuels 19, 216-223.
Yu, J., Liu, N., Li, L., Lee, R.L., 2012. Generation of nanoparticle-stabilized supercritical CO2 foams, Carbon Management Technology Conference. Carbon Management Technology Conference.
Zhang, C., Oostrom, M., Wietsma, T.W., Grate, J.W., Warner, M.G., 2011. Influence of viscous and capillary forces on immiscible fluid displacement: Pore-scale experimental study in a water-wet micromodel demonstrating viscous and capillary fingering. Energy & Fuels 25, 3493-3505.
Zheng, X.L., Mahabadi, N., Yun, T.S., Jang, J., 2017. Effect of capillary and viscous force on CO2 saturation and invasion pattern in the microfluidic chip. Journal of Geophysical Research-Solid Earth 122, 1634-1647.